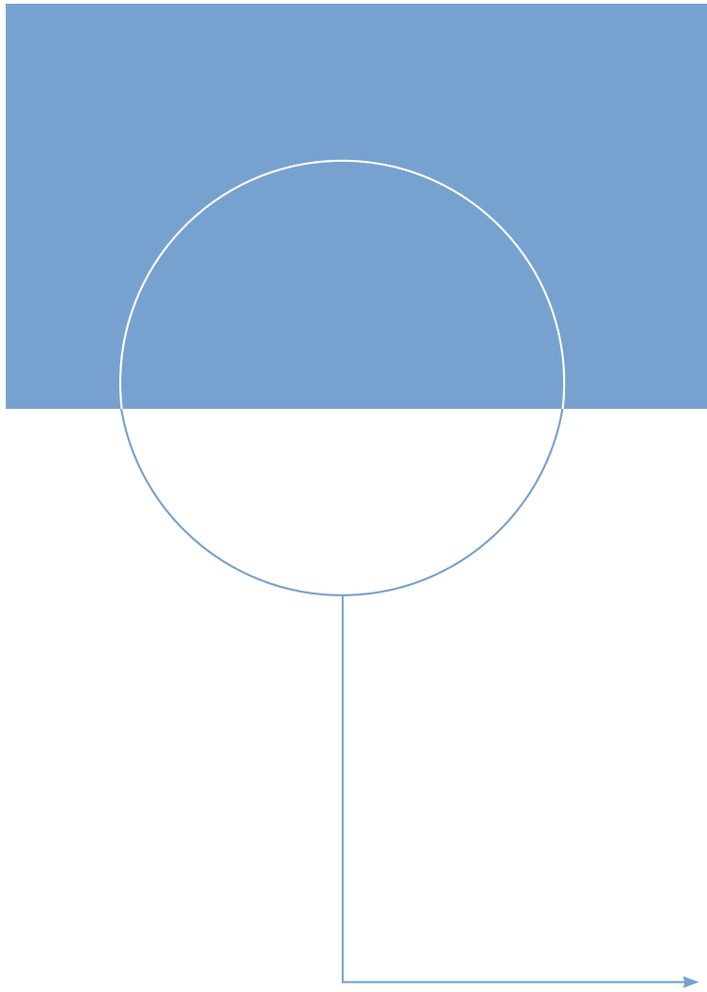

Master's thesis

2019

Nora Plassbak Sagatun

NTNU
Norwegian University of Science and Technology
Faculty of Information Technology and Electrical Engineering
Department of Electric Power Engineering

Nora Plassbak Sagatun

Battery Based Energy Storage Emulation in Low Voltage Grids

June 2019

NTNU
Norwegian University of Science and Technology

NTNU
Norwegian University of Science and Technology

NTNU
Norwegian University of
Science and Technology

Battery Based Energy Storage Emulation in Low Voltage Grids

Nora Plassbak Sagatun

Master of Energy and Environmental Engineering
Submission date: June 2019
Supervisor: Elisabetta Tedeschi
Co-supervisor: Santiago Sanchez

Norwegian University of Science and Technology
Department of Electric Power Engineering

Preface

This master thesis concludes my five years degree in Energy and Environmental Engineering at the Norwegian University of Science and Technology. I would like to thank my co-supervisor Post-Doctor Santiago Sanchez for his help and support with both the simulation models and the laboratory work. Moreover, I want to thank my supervisor Professor Elisabetta Tedeschi for her support on the topic, as well as great advice regarding the structure of the thesis. My supervisor and co-supervisor also encouraged me to write an academic paper with the most important findings and results from this thesis. The paper is written as a contribution to the EEEIC conference in Genoa, Italy, June 2019, a conference I will attend to present the findings. The academic paper is attached to the appendix of this thesis.

Furthermore, I benefited from debating the issues of my thesis with my friends at NTNU. It has been a pleasure to share my victories and frustrations with you. Lastly, I want to thank my family for their encouragement, and for proofreading the thesis. Thank you.

Trondheim, June 2019
Nora Plassbak Sagatun

Summary

The electrical grid is in the midst of a significant transition. One of the most important trends which modernizes the grid is the increased penetration of distributed energy resources. Distributed generation causes for bidirectional power flow and a decentralized grid design. The integration of renewable energy sources comes with challenges, especially in regards to planning and operation. The challenges are primarily due to the intermittent characteristics of renewables, as they are usually weather dependent. The integration of energy storage systems to the low voltage grid supports the use of renewable energy sources.

The work of this thesis concerns the grid integration of a battery energy storage system. The components involved in the system are described theoretically. Moreover, the battery pack is designed to fulfill the set requirements and tested computationally. A DC-DC converter is presented with an outline of the inner current control and outer voltage control. The battery and converter are implemented in the MATLAB/Simulink environment, and the results are presented. Further, the power hardware in the loop (PHIL) methodology is explained. The battery pack and DC-DC converter are combined with a physical grid connection using a physical voltage source converter by employing the PHIL technique. The emulation of the energy storage system is presented through the laboratory results.

The work of the thesis can be split up in three main parts: design, simulation, and laboratory work. The design process includes designing the battery storage system. Different battery types are outlined, and the lithium-ion battery is chosen. Further, the battery ratings are designed in correspondence with given requirements and rated data for the lithium-ion battery. The DC-DC converter components are designed, as well as the current and voltage control. The simulation process gives the results from the battery and DC-DC converter modeled as an average model. The laboratory work implements the power hardware in the

loop methodology to connect the battery energy storage emulation to physical laboratory equipment.

The computational results showed a functioning control strategy for both the voltage and current control loops. The DC-DC converter and the battery provided acceptable voltage and current outputs, which enabled the further laboratory testing. From the laboratory work, the voltage and current responded quickly, and the simulated and physical sensor voltage behaved identically. The current from the physical equipment experienced a higher level of noise than the simulated current, due to the use of sensors rated to much higher currents, leading to a sensitive low current operation. To summarize, this thesis presents a functioning power hardware in the loop strategy for the emulation of an energy storage system connected to a low voltage grid.

Sammendrag

Det elektriske nettet er i ferd med å moderniseres betydelig. En av de mest vesentlige trendene som kan modernisere kraftnettet er økt penetrasjon av distribuerte energiressurser. Distribuert generasjon forårsaker bidireksjonal kraftflyt og et desentralisert nettdesign. Integrasjonen av fornybare energikilder kommer med utfordringer, særlig når det gjelder planlegging og drift. Dette skyldes hovedsakelig de periodiske egenskapene ved fornybar energi, da de ofte er væravhengige. Integrasjonen av energilagringssystemer til lavspenningsnettet støtter bruken av fornybare energikilder.

Denne avhandlingen tar for seg netteverksintegrasjonen av et batteri energilagringssystem. Komponentene som er involvert i systemet beskrives teoretisk. Batteripakkene er designet for å møte de gitte kravene og testes gjennom simuleringer. En DC-DC omformer presenteres med en forklaring av indre strømløkkeregulering og ytre spenningsløkkeregulering. Batteriet og omformeren er implementert i MATLAB/Simulink, og resultatene presenteres. Videre forklares power hardware in the loop (PHIL) metoden. Batteripakken og DC-DC omformeren kombineres med en fysisk nettforbindelse ved bruk av en spenningskildeomformer ved å benytte PHIL-teknikken. Emuleringen av energilagringssystemet presenteres gjennom laboratorieresultatene.

Arbeidet i denne avhandlingen kan deles opp i tre hoveddeler: design, simulering og laboratoriearbeid. Designprosessen omfatter å utforme batterisystemet. Ulike batterityper er skissert, og litium-ionbatteriet er valgt. DC-DC omformerens komponenter er kalkulert, samt en regulering av strøm og spenningskontroll. Simuleringsprosessen gir resultatene fra batteriet og DC-DC omformeren modellert som en gjennomsnittsmodell. Laboratoriearbeidet implementerer PHIL strategien for å koble det emulerte batterilagringssystemer til fysisk laboratorieutstyr.

Simuleringsresultatene viste en fungerende kontrollstrategi for både spennings- og strømkontrollsløyfene. Spenningene og strømmene ut av batteripakken og DC-DC omformeren var akseptable. Dette muliggjorde videre laboratorietesting. Eksperimenter i laboratoriet viser at den simulerte og fysiske sensorspenningen oppførte seg identisk. Strømmen fra det fysiske utstyret opplevde et høyere støynivå enn den simulerte strømmen, noe som bunner i bruken av sensorer som er vurdert til mye høyere strømmer som fører til en sensitiv lavstrømsdrift. For å oppsummere, presenterer denne oppgaven en fungerende PHIL strategi for emulering av et energilagringssystem koblet til et lavspenningsnett.

Contents

List of Figures

Abbreviations

AC	=	Alternating Current
BESS	=	Battery Energy Storage System
CIL	=	Controller in the loop
DC	=	Direct Current
DER	=	Distributed Energy Resource
DG	=	Distributed Generation
DOD	=	Depth Of Discharge
DSO	=	Distribution System Operators
DUT	=	Device Under Testing
ESS	=	Energy Storage System
FACT	=	Flexible AC transmission system
FPGA	=	Field-Programmable Gate Array
GFC	=	Grid Forming Converter
HIL	=	Hardware In The Loop
HV	=	High Voltage
IEC	=	International Electrotechnical Commission
IEEE	=	Institute of Electrical and Electronics Engineers

IGBT	=	Insulated Gate Bipolar Transistor
KCL	=	Kirchhoff's current law
KVL	=	Kirchhoff's voltage law
LTC	=	Load Tap Changer
MG	=	Microgrid
MMC	=	Modular Multi-level Converter
MOSFET	=	Metal-Oxide Semiconductor Field-Effect Transistor
PHIL	=	Power Hardware In The Loop
PI	=	Proportional-Integral
PID	=	Proportional-Integral-Derivative
PLL	=	Phase Locked Loop
PV	=	Photovoltaic System
RTS	=	Real Time Simulation
SOC	=	State Of Charge
UAV	=	Unmanned Aerial Vehicle
VSC	=	Voltage Source Converter
VSM	=	Virtual Synchronous Machine

Chapter 1

Introduction

1.1 Background and Motivation

The electrical grid is in the midst of a significant transition. As the world's population continues to grow, more people require electricity as well as the ever attention to climate change mitigation is growing [1; 2]. At present, the traditional distribution grid typically has a centralized design with unidirectional power flow. A centralized power system is structured with large power plants based on, among others, hydropower or oil and gas which feed power to the transmission system which further distributes the power to distribution grids and end-users, as illustrated in figure 1.1.

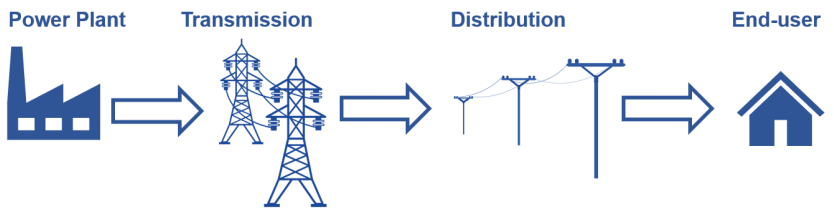

Figure 1.1: Simplified illustration of a traditional power system

One of the most significant trends which modernizes the grid is the increased penetration of distributed energy resources. Distributed generation causes for bidirectional power

flow and a decentralized grid design [3], which is made evident in figure 1.2. This leads to an increased concern for the control of distribution grids.

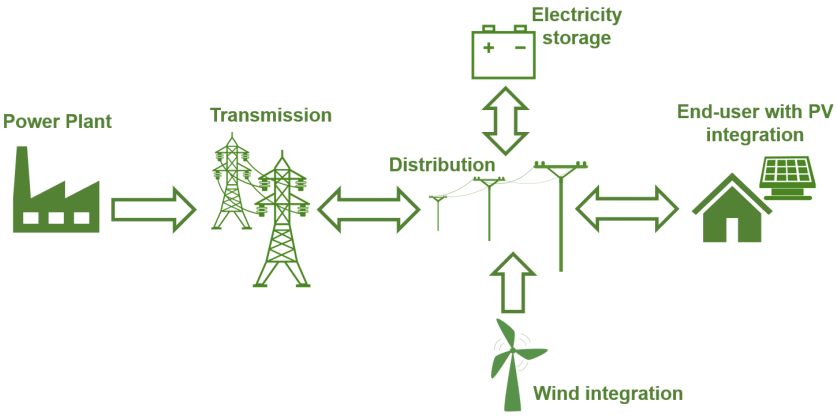

Figure 1.2: Simplified illustration of a modern power system

The motivations for implementing distributed generators in the power system lead to several benefits and challenges. The implementation can result in lower power prices, higher reliability, decreased emissions of greenhouse gases, and the alleviation of poverty in regions where electricity is not necessarily a given. Higher penetration of distributed energy resources will also initiate lower transmission losses and higher flexibility of the grid. However, when a distributed generator is connected to the distribution grid, it leads to complicated control and regulation to avoid challenges regarding, for instance, voltage fluctuations and negative externalities on power quality [4]. Consequently, power electronics will be an efficient and reliable interface to the grid [5].

The integration of renewable energy sources comes with challenges, especially in regards to planning and operation. The challenges are primarily due to the intermittent characteristics of renewables, as they are usually weather dependent. The integration of energy storage systems (ESSs) to the low voltage grid supports the use of renewable energy sources. When the renewables experience peak generation, the energy storage system enables for a storing of the excess energy, and when the renewables experience weather

challenges such as cloud cover or no wind, the ESS can distribute the stored energy to the power grid. This is one of many advantages with the connection of ESS to a low voltage grid. Other advantages include power quality improvement, peak shaving, cost reduction, and mitigation of greenhouse gases.

Most power electronic converters used for grid interfacing of distributed generation have a unidirectional power flow. However, to enable for charging and discharging of a battery energy storage system (BESS), a bidirectional power flow converter is required. Conventionally, an independent buck converter and an independent boost converter can be used in parallel to achieve the bidirectional power flow. However, the demand for complex control, as well as compact and efficient grid integration works in favor of the bidirectional converter. A bidirectional DC-DC converter is widely used in the ESS application, particularly in low voltage grids in the range of 50 to 1000 V AC. The bidirectional converter connects the energy storage technology to an additional converter that links the DC side with the AC grid. It supports the step up of a voltage from the battery side to a grid side, as well as stepping down the voltage in the opposite direction. This leads to improved performance of the system as the converter allows for an efficient control of the voltage levels [6; 7].

1.2 Problem Definition

The work of this thesis concerns the grid integration of a battery energy storage system. The components involved in the system are described theoretically. Moreover, the battery pack is designed to fulfill the set requirements and tested computationally. A DC-DC converter is presented with an outline of the inner current control and outer voltage control. The battery and converter are implemented in the MATLAB/Simulink environment, and the results are presented. Further, the power hardware in the loop (PHIL) methodology is explained. The battery pack and DC-DC converter are combined with a physical grid connection using a physical voltage source converter by employing the PHIL technique. The emulation of the energy storage system is presented through the laboratory results.

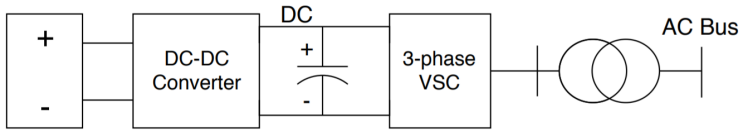

Figure 1.3: Line diagram of paper scope

The aim of this thesis is to develop an emulation of a battery energy storage system in a low voltage grid connection conducted with a power hardware in the loop methodology. The aim will be achieved by reaching the following objectives:

1. Design and study a battery energy storage system.
2. Investigate and describe a DC-DC converter and design its current and voltage control.
3. Review the power hardware in the loop concept and create a structure suitable for an energy storage system emulation.
4. Develop a simulated computational model for testing of the battery pack and DC-DC converter to review the design and control setup.
5. Implement the power hardware in the loop structure with the simulated model in a real-time simulation connected with physical laboratory equipment to obtain an emulation of the battery and DC-DC converter in connection with a physical low voltage grid.

1.3 Methodology

The methodologies used in this thesis include:

- Analytical calculations are used in the design process of the thesis. The battery design is conducted using the analytical calculations to size the battery to fulfill the set requirements. Further, the components of the DC-DC converter, as well as the tuning of the converter's PI regulators are attained from analytical calculations.

- Computational simulation is used to test the energy storage system with the DC-DC converter. The simulations are used to confirm a functional control strategy, as well as to confirm the desired voltage output. Further, the simulation model tests the discretization algorithm and the impact of noise in the system.

- Power hardware in the loop laboratory setup is the final methodology used in the thesis. The technique involves the simulated computational model implemented in a real-time simulator with the connection of physical laboratory equipment of a voltage source converter and a digital amplifier.

1.4 Relation to Specialization Project

The primary objective of the specialization project [8] was to review microgrids and the contribution of microgrids to the shift towards a modern power system, to investigate and to describe the current and voltage control of voltage source converters (VSCs) which are integrated in an islanded grid, to analyze the hierarchical structure of droop based control of microgrid and describe the algorithmic approach for the roles in the control and lastly to develop a model in Simulink for testing of a microgrid structure which investigates some of the theoretically explained control strategies. Even though this thesis has pivoted into a more focused direction of a power hardware in the loop emulation of an ESS, the specialization project functioned as a good basis for the work. The voltage source converter control is not included in this thesis as the VSC included in the scope is a physical laboratory converter and not a part of the simulation model.

Parts of section 1.1 from the introduction are based on the specialization project. Further, in chapter 2, section 2.1 and 2.5 are strongly based on [8]. As the voltage source converter held a primary role of the specialization project, parts of that information is collected in section 2.4. The thesis could potentially be combined with the models from the specialization project to obtain an all-around adaptable model for testing of microgrid operation. This proposal is in detail described in chapter 8, Further Work.

1.5 Limitation of Scope

The problem definition and scope open for several interesting focus areas. However, as the objectives for the thesis includes both computational modeling and laboratory work, the limitation of the scope was necessary due to time constraints. The scope covers the process of discharging the battery to the distribution grid. The charging of the battery from the grid is excluded from the scope. However, the charging of the battery model is included in appendix B, but without the DC-DC converter. The bidirectionality of the DC-DC converter is excluded from the scope due to time constraints. This causes the DC-DC converter to act as a unidirectional boost converter, which is what it is modeled as in this thesis. The scope includes a physical voltage source converter from the laboratory. Thus this is not modeled computationally. However, the modeling and control of a voltage source converter was the scope of the specialization paper leading up to this thesis. This also leads to the constraint on components. Other grid components that could be supported by the ESS, such as PV, wind turbines, or loads are not included in the scope of the thesis. Moreover, other energy storage technologies than batteries are mentioned, but not studied in detail. The scope includes an outline of different rechargeable battery types, but only lithium-ion is used further for testing. The DC-DC converter is tested as an average model; the switching model is mentioned but not described in detail.

1.6 Structure of Thesis

This thesis is structured with sections enumerated as X.Y.Z.A where X is the number of the chapter, Y is the number of the section, Z is the number of the subsection, and A is the number of the subsubsection within the chapter X. Tables and figures are expressed as X.Y, where Y is the number of the figure or table, while X is the number of the chapter where the figure or table is inserted. Equations are expressed on the form (X.Y), and as with figures, X is the number of the chapter and Y is the number of the equation in chapter X. References are cited in the text with square brackets [], and are listed according to the IEEE citation style.

Chapter 2 gives the reader a qualitative description of the system components considered in the thesis as well as it provides context for the motivation of the thesis scope. The terms discussed are distributed generation, energy storage systems, bidirectional DC-DC converters, voltage source converters, and microgrids.

Chapter 3 describes the battery system. This includes an outline of different battery types and a more detailed description of the use of lithium-ion used in a battery energy storage system. Further, the battery model is described and designed. Lastly, the chapter presents the implementation of the battery pack in Simulink.

Chapter 4 presents the DC-DC converter used further in the thesis. The boost converter topology is described and analyzed, and the average model is presented. Section 4.3 includes the converter control with the inner current control loop and outer voltage control loop, as well as the tuning of the PI regulators used.

Chapter 5 presents the concept of power hardware in the loop. Further, the chapter describes the applications of hardware in the loop and power hardware in the loop for different tests and across a number of industries. The chapter provides the PHIL structure used in the thesis, as well as the discretization algorithm later used to support this testing methodology.

Chapter 6 provides the computational results obtained from the simulation process. The battery system and DC-DC converter is implemented in a MATLAB/Simulink model and tested to analyze the functionality of the control as well as the voltage and current output. The chapter includes the results from the battery pack with the voltage and current output, state of charge, and discharge curve. Further, the discretized model is presented, with and without the implementation of noise in the model. Lastly, the chapter includes a discussion of the computational results.

Chapter 7 presents the laboratory work conducted in the thesis. The chapter includes information about the laboratory and the components used, the current and voltage results from the PHIL laboratory tests as well as a discussion of the results.

Chapter 8 provides the concluding remarks from the thesis and the proposals for further work.

Chapter 2

Components and Definitions

The purpose of this chapter is to give a qualitative description of the system considered in the thesis. This includes a presentation of the terms distributed generation (DG), energy storage system (ESS), bidirectional converter, and voltage source converter (VSC). As these components all can be combined to form a functional microgrid, this is also a concept studied in this chapter. A description of the role of power electronic interfaces in a microgrid is included.

There is a long way between the traditional grid structure and a smarter, greener, and more efficient modern grid. These steps include the connection of more distributed generation, with the environmental aspects of renewable energy sources as well as the low transmission losses. Further, the connection of energy storage systems causes numerous advantages in a grid with a high penetration of distributed generation. In the control and stability of the grid, the connection of power electronic converters as bidirectional DC-DC converters and voltage source converters holds an important role. A microgrid consisting of the above-mentioned components can prove to be both more efficient, more reliable, and a grid with less emissions than the tradition grid structure.

2.1 Distributed Generation

There are several ways of defining distributed generation. The issues defining DGs include the purpose, the location, the rating of DG, the power delivery area, the technology, the environmental impact, the mode of operation, the ownership and the penetration of DG [9]. However, all of these factors might not be relevant to this thesis, hence the definition chosen for this paper uses more general terms: distributed generation refers to small generating units and the joint energy storage and power generation systems installed at the user end, which meet specific user needs. DGs are limited to scale of a few dozen kilowatts to tens of megawatts [10]. In this report, DGs are given in kilowatts.

The technology behind DGs is based on renewable energy sources (RES), non-renewable electricity generators, and energy storage systems (ESS). Common renewable energy sources used in distributed generation may include photovoltaic systems (PV) and wind energy systems. Distributed energy resources (DER) also include controllable loads such as plug-in vehicles and power electronic loads [11]. The grid can take advantage of ancillary services provided by the increasing popularity of electric vehicles [12]. Typical non-renewable DGs are diesel engine generators, single shaft microturbines, and reciprocating engines [13]. Solid oxide fuel cells can be both categorized as a renewable and a non-renewable DG, depending on where the hydrogen comes from. Battery systems and hydrogen storage systems, as well as flywheel systems are primarily used as ESS [14; 15].

2.2 Energy Storage Systems

The term energy storage implies the capture of energy which is produced at one time, but can be used at a later time. The implementation of energy storage systems in low voltage grids is becoming more popular, usually to support power distribution with renewable energy sources. However, implementation of ESSs has numerous other advantages. Some of them are listed below with a short explanation or example of application [16].

- **Power quality improvement** The challenge regarding power quality problems in distribution networks can appear as voltage drops, dynamic voltage increase, or harmonic pollution. A distribution grid connected ESS can provide an output of active and reactive power, while simultaneously maintain a four-quadrant operation. This leads to the ESS as an important factor of power quality management of distribution grids. [17; 18; 19].

- **Mitigation of voltage deviation** Over-voltages are a common issue observed with the integration of PVs to the grid. Distribution systems usually include on-load tap-changing transformers (LTC) at the substation for the control of the network voltage magnitude within rated limits. Previously, in the traditional grid structure, DSOs could set the limits of the LTCs sufficiently high to ensure voltage within the limits. This proves more difficult for PVs as the output happens at a low demand area such as a residential area in the middle of the day. This can cause overvoltages exceeding the limits. With the increasing integration of PVs in the grid, one single tap setting of a voltage regulator would unlikely maintain a voltage level acceptable to the end feeder. Further, varying cloud cover can complicate the voltage control more, which can cause fluctuating voltages. ESSs enable the mitigation of many of these unwanted impacts of PVs. Most of the ESS methods of obtaining this change is through the utilization of real and reactive power injections and absorption [20; 21].

- **Frequency regulation** The advantage of frequency regulation by energy storage systems are especially important in isolated microgrids. A battery energy storage system (BESS) device effectively reduces the peak frequency deviations with the provision of fast active power compensation [22].

- **Load leveling and peak shaving** Peak shaving refers to the technique of mitigating the effects of large energy loads during a certain period by either advancing or delaying its effects before the power system can accept the load. With the implementation of ESS, the system can be charged when the supply system is experiencing minimal load. When the energy load is high (such as at its peak), it is discharged to provide additional power [23].

- **Facilitation of renewable energy source (RES) integration** With the intermittent behavior of RESs like PV and wind turbines, ESS can be used to shift the generation from the renewable energy source to be used when the demand requires it. When the RESs experience peak generation, the ESS enables for a storing of the excess energy. When the RESs are not in the condition to generate sufficient power, the ESS can distribute the stored energy [24].

- **Cost reduction** Implementing ESS in low voltage grids can lead to cost reduction in numerous ways. One of the services the ESS can provide which leads to cost reduction is the process of peak shaving. The ESS can be charged at a time of day when the system load is low, as well as the electricity prices. When the ESS feeds this power to the system at a high load high priced time of day, this leads to a decline in costs for end-users [23].

- **Operating reserves** Many ESSs as batteries, capacitors, and flywheels interact with the capability of serving operating reserves such as the spinning reserve. The spinning reserve is the generation capacity that is on the line. The reserve is unloaded and can relatively quickly respond to compensate for generation or transmission outages. A grid-connected ESS can also have a supplemental reserve for the generation which might be off-line, as well as backup supply which works, as the name implies, as a backup for the other reserves. The backup reserve has the slowest respond time [25].

2.3 Bidirectional DC-DC Converter

A bidirectional DC-DC converter is a converter that enables bidirectional power flow. A grid-connected bidirectional DC-DC converter can both provide power to the grid and the converter connected component. Bidirectional energy transfer has become a well-established part of numerous modern power conversion systems [6]. This makes the technology especially suitable for a grid-connected ESS. Bidirectional converters enable the increasing and decreasing of voltage for maintaining a stable power flow [7]. This type of converter is the main device used to interface a battery or supercapacitor, because it

can convert the low DC voltage from the battery to a higher DC voltage to the grid when the battery discharges, as well as it converts the high side DC voltage from the grid to the low DC battery voltage when the battery system is charging [26]. This increases system reliability. Bidirectional DC-DC converters are also used in electric vehicles for capturing the kinetic energy of the motor and charging the battery during the regenerative braking by the reverse power flow of energy [27]. Figure 2.1 illustrates the bidirectional power flow of a DC-DC converter. The bidirectionality is realized through the use of two unidirectional semiconductors. These include transistors, MOSFET, and IGBT power switches with parallel diodes. The diodes in parallel enable the two-sided power flow.

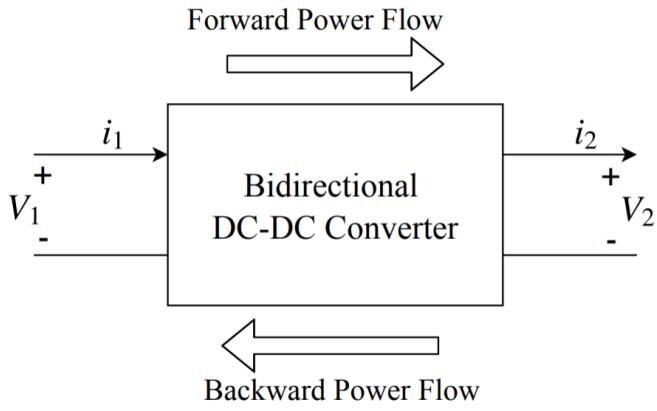

Figure 2.1: Illustration of a bidirectional converter.

2.4 Voltage Source Converter

The power system is dependent on control of both power and voltage to ensure stability and reliability, which might be a challenge when loads and generators are varying. A voltage source converter (VSC) works in favor of the superior control, due to among others, its modularity, independence of the AC network, the independent control of active and reactive power, the low power operation and the power reversal [28]. The voltage source converter can generate variable voltage and frequency AC output from a constant frequency, DC voltage source [29]. The two-level VSC is the simplest form of a three-phase VSC. This type can be compared to a six pulse bridge, but with two significant tweaks.

The first is the replacement of the thyristors with insulated-gate bipolar transistors (IGBT) with a parallel inverse diode. The second is the replacement of the reactors with capacitors on the DC-side. VSCs also comes in the form of more complicated three-level converters and modular multi-level converters (MMCs). VSCs are widely used in power systems for distributed generation, HVDC applications, and back to back systems. VSCs provide voltage regulation and harmonic compensation as required for the system [30]. Further, VSCs can provide ancillary services such as reactive support by generating units and loads [31], and can control a seamless power supply from intermittent DERs [32]. Figure 2.2 shows the topology of a two-level voltage source converter used as a rectifier.

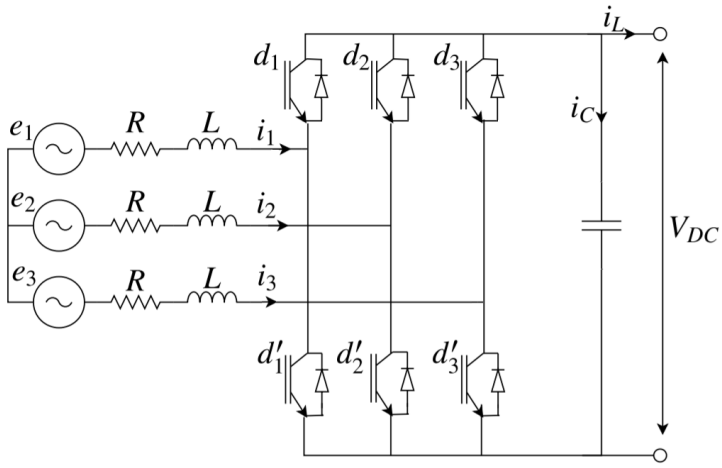

Figure 2.2: Voltage Source Converter topology used as a rectifier

2.5 Microgrid

Prior to the process of defining a microgrid (MG), distribution grids and low voltage (LV) power systems needs to be defined. The distribution grid is a part of the transmission system which distributes power from the regional grid to the consumer through both high voltage and low voltage lines. For the use of electricity in buildings, the voltage needs to be transformed down to low voltage. International standards for electrical power systems generally define low voltage to be beneath 1000 V. The low voltage supply system is by International Electrotechnical Commission (IEC) defined as the voltage in the range 50 to

1000 V AC or 120 to 1500 V DC in *60038:2009 IEC Standard Voltages*.

For the purpose of this thesis, the microgrid definition from the EU research project [33; 34] is used:

> Microgrids comprise LV distribution systems with distributed energy resources (DER) (microturbines, fuel cells, PV, etc.) together with storage devices (flywheels, energy capacitors and batteries) and flexible loads. Such systems can be operated in a non-autonomous way, if interconnected to the grid, or in an autonomous way, if disconnected from the main grid. The operation of microsources in the network can provide distinct benefits to the overall system performance, if managed and coordinated efficiently.

In other words, a microgrid is a low voltage distribution system with a cluster of distributed energy resources, ESSs and loads [35]. A microgrid system can operate either connected or disconnected from the main grid. It has clear electrical boundaries and acts as one single controllable entity with respect to the main grid. The operation of distributed generators in the network can improve the system performance of the entire grid system if it is managed and coordinated successfully [36; 37].

There are several advantages to implementing MGs [38; 39]. The implementation will contribute to the shift to smarter grids and will work as a beneficial solution for pilot projects, which enables testing of modern smart grid technologies [40]. As mentioned previously, MGs provide a solution to more efficiently integrating DERs [41; 42]. Moreover, from the end user perspective, increased reliability can be experienced, as the MG can switch to islanded mode if a fault is detected in the main grid. With DGs and autonomous control structures, microgrids alleviate the dependency and consequently, the pressure on the transmission system. With local generation of energy, distribution losses and costs will decrease. However, the implementation of MGs also causes challenges. It is essential that a grid ensures reliable operation and control, which in the case for MGs might be more demanding. For instance, there are challenges regarding the start-up of island mode, as well as the balancing of generators and loads [43]. The ESSs required for the MGs need to be

adequate and reliable, and there are challenges with regards to the balancing of generation and loads when the demand is uncertain, as well as the scale of the reserve [40]. There is also a challenge regarding the components, as it must be confirmed that all components are compatible with each other.

Chapter 3

Battery Energy Storage System

This chapter will provide a thorough explanation of the modeling of a battery pack, as well as the computational model later used in Simulink. Section 3.1 provides an outline of rechargeable battery types, and describes a lithium-ion based BESS. Section 3.2 explains the computational battery model characteristics. Section 3.3 presents the calculation, which leads to the final battery system design, which is further used in this thesis. The last section discusses how the battery behaves in the MATLAB/Simulink environment through a computational implementation.

In the aim of matching the grid electricity supply with the demand, energy storage systems are essential. However, in a well-operated grid, this is not the only role of an ESS. In a low voltage grid, a BESS can contribute significantly in the frequency regulation and in maintaining stability in the grid [44; 45]. Further, energy storage can store available energy for consumption at a more beneficial time, as well as for the case of emergencies [46]. This causes for peak load reduction. BESS implementation also enables the provision of ancillary services to networks. These advantages lead to a more efficient use of RES, which contributes to economic benefits [47]. The most researched energy storage technologies include batteries, supercapacitors, and flywheels [48]. This thesis will focus on the application of a battery energy storage system.

3.1 Battery Energy Storage System Technologies

3.1.1 Outline of Battery Types

There are mainly four major secondary battery technologies, Lead-Acid, Lithium-Ion (Li-Ion), Nickel Cadmium (NiCd) and Nickel-Metal-Hydride (NiMH) [49]. The battery type used in further in this thesis is the Li-ion battery. This section will defend this decision as well as give a short comparison between the options.

Nickel Cadmium batteries are a cost-efficient battery type [50]. The model provides more watt-hours of operation than the other types per shift. Further, NiCd performs well even under extreme circumstances, both in severely cold and warm temperatures. The NiMH battery type holds the advantage of providing a remarkable operation life between charges [51]. The battery design of NiMH holds an operation time of 30-40$\%$ longer than of NiCd. However, NiMH has a more inferior operation under extreme temperature conditions. Lead-Acid batteries hold some similarities to NiCd [52]. The battery type has a lower price, but requires more maintenance and have a shorter operation time. Furthermore, Lead-acid batteries, as NiMH have a weaker operation in both high and low temperatures.

A significant drawback of various battery types is their susceptibility to the memory effect. This causes the battery to *remember* the discharge depth, which in turn reduces the effective capacity of the battery. The memory effect affects battery types as NiCd, NiMH, NiO(OH) and $Ni(OH)_2$ [53]. Therefore, the types require a periodic discharge to be sure that the memory effect is not exhibited. This induces a significant decrease in work voltage capacity. The memory effect does not apply to Li-ion or Lead Acid, which leads to more straightforward maintenance procedures and lower cost of preservation resources [54; 55].

A further advantage of the Li-ion battery is its characteristic of having a high energy density, causing it to be a leading battery type in appliances as electronics, electric vehicles, and renewable energy sources [56]. Moreover, Li-ion batteries have a significantly lower

self-discharge rate than both NiCd and NiMH forms. A third advantage of the Li-ion battery type is the lack of required maintenance to assure an acceptable operation.

3.1.2 Lithium-Ion based BESS

Lithium-ion technology based BESS is increasingly popular. This is due to its advantages mentioned above, as well as other characteristics. These include high cycle efficiency, low self-charge, high nominal cell voltage, and long life cycle. The charging process of lithium-ion batteries can be intermittent, and the process is more advanced for the nickel-based battery types. These assets lead to the lithium-ion battery to be suitable for storing renewable energy such as wind or solar energy.

A commitment to a lithium-ion based BESS leads to some safety measures to prevent damage [57; 58]. These measures include a control system for the management of depth of discharge (DOD), an integrated safety valve, and a vent that opens when the temperature exceeds a certain point. DOD is another method of expressing the battery's state of charge (SOC), which are complementary values. Further in this thesis, the term state of charge will be used. The BESS requires a control system that can manage the SOC of the battery because the SOC of a lithium-ion battery is affecting the life cycle of the battery [59]. There should be an integrated safety valve in the battery to stabilize the pressure in a cell when it experiences an overcharge. That is when the cell is charged to a voltage level over the design specifications. The cells of the battery can also undergo over-discharge, when the cell is discharged to a voltage level below the rated specifications. Lithium-ion batteries are fragile and the stability of the battery can be reduced with low and high temperatures. The temperature rise in a lithium-ion battery cell can be divided into three states. The first and second stages are the onset and acceleration, respectively. The third stage is called thermal runaway, which will lead to a rapid rise in temperature, and flame [60]. Therefore, most batteries include a vent that opens when the temperature exceeds a specific limit. This prevents the battery from exploding. When the vent has opened, the battery is no longer usable.

3.2 Battery Model

This section explains the development of the battery model. The computational model and its behavior are presented.

3.2.1 Computational Battery Model

The state of charge (SOC) of the battery can be expressed as in equation (3.1) [61; 62]. The SOC is ranging from 1 (fully charged) to 0 (fully discharged).

$$SOC = (1 - \frac{\int i_b dt}{Q}) \tag{3.1}$$

Where i_b is the battery current, and Q is the battery capacity. The terminal voltage v_b is calculated as shown in equation (3.2). The open circuit voltage is expressed as E_0. The internal resistance is denoted R_b. K denotes the polarization voltage. A and B are the exponential zone voltage and the exponential capacity respectively.

$$v_b = E_0 + R_b \cdot i_b - K\frac{Q}{Q + \int i_b dt} + A \cdot exp(-B \int i_b dt) \tag{3.2}$$

$\int i_b dt$ is the actual battery charge, in Ampere-hours (Ah), the same unit as the capacity. The three model parameters A, B and K can be derived by the end of the exponential zone (V_{exp} and Q_{exp}), the fully charged voltage (E_{full}) and the end of the nominal zone (E_{nom} and Q_{nom}) [49]. The exponential zone voltage is given in equation (3.3) with the unit V.

$$A = E_{full} - E_{exp} \tag{3.3}$$

The exponential capacity is given in (3.4) in $(Ah)^{-1}$

$$B = \frac{3}{Q_{exp}} \tag{3.4}$$

Equation (3.5) presents the polarization voltage K in volts.

$$K = \frac{(E_{full} - E_{nom} + A \cdot (exp(-B \cdot Q_{nom}) - 1)) \cdot (Q - Q_{nom})}{Q_{nom}} \tag{3.5}$$

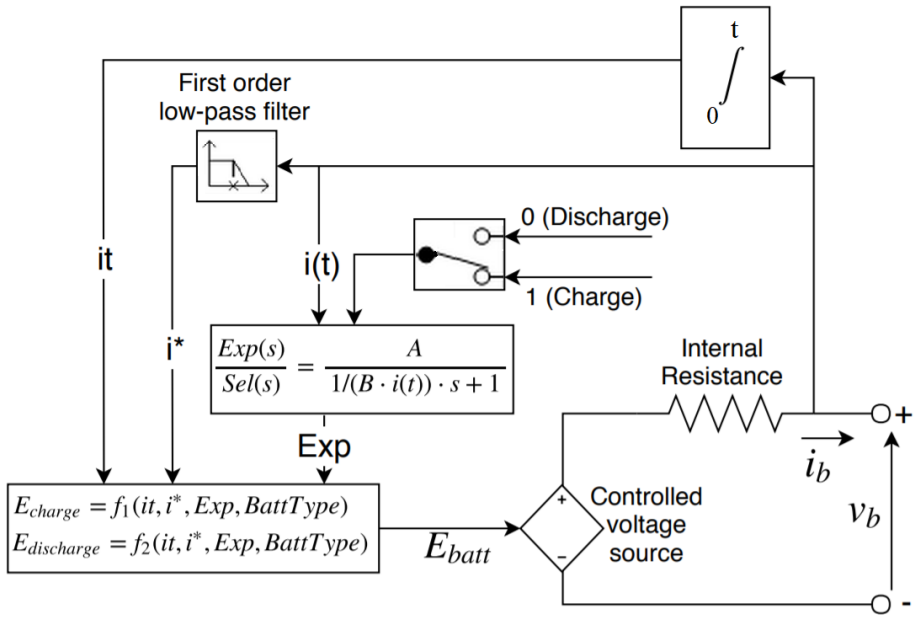

Figure 3.1: Equivalent battery model from Simulink.

In the conceptual scheme in figure 3.1, E_{batt} is the nonlinear voltage. $Exp(s)$ denotes the exponential zone dynamics and $Sel(s)$ represents the battery mode, where $Sel(s) = 0$ when the battery is discharging and 1 when the battery is charging. $i*$, i_b and it are respectively the low frequency current dynamics, the battery current and the extracted capacity [63].

The discharge model of the Lithium-Ion battery is given as in equation (3.6) and the charge model is given in (3.7).

$$f_1(it, i*, i) = E_0 - K \cdot \frac{Q}{Q - it} \cdot i* - K \cdot \frac{Q}{Q - it} \cdot it + A \cdot exp(-B \cdot it) \tag{3.6}$$

$$f_2(it, i*, i) = E_0 - K \cdot \frac{Q}{it + 0.1 \cdot Q} \cdot i* - K \cdot \frac{Q}{Q - it} \cdot it + A \cdot exp(-B \cdot it) \tag{3.7}$$

3.2.2 Internal Resistance

The battery's internal resistance has a significant impact on the voltage drop caused by the current deviation. Reference [49] discovered a mismatch between the internal resistance provided by the manufacturer's data sheet and the current variation. Therefore, a new relation was proposed as in equation (3.8).

$$\eta = 1 - \frac{I_{nom} \cdot R_b}{V_{nom}} \tag{3.8}$$

Where η is the efficiency coefficient. The nominal discharge curve is dependent on the rated current, I_{nom}, which therefore can be expressed as in equation (3.9). From the datasheet [64], it is remarked that the standard discharge of the battery after a standard charge is given at 0.2.

$$I_{nom} = Q_{nom} \cdot 0.2/1hr \tag{3.9}$$

Which results in the final equation of efficiency:

$$\eta = 1 - \frac{0.2 \cdot R_b \cdot Q_{nom}}{V_{nom}} \tag{3.10}$$

Rewriting equation (3.10) gives the internal battery resistance expressed from the nominal voltage, the efficiency and the nominal capacity.

$$R_b = V_{nom} \cdot \frac{1 - \eta}{0.2 \cdot Q_{nom}} \tag{3.11}$$

3.3 Battery Design

After choosing the battery type and studying the battery model, the battery can be designed. The design of the battery pack is based upon data sheet [64]. The battery system is modeled to supply a load of 15 kW for 5 hours. The output voltage v_b is modeled to 96 V and is intended to be connected to a boost converter. However, as the design implementation in Simulink was a significant part of achieving the objectives of the thesis, the step by step procedure followed was the modeling of two identical batteries in series with

the output voltage of 48 V. Therefore, this section presents the design of one of these two identical batteries.

The nominal voltage of one battery cell is given at 3.7 V. The output voltage is dependent on the number of battery cells connected in series. The number of batteries in series n_s is calculated as the fraction of the total battery voltage and the voltage of one battery cell as in (3.12).

$$n_s = \frac{48}{3.7} = 12.97 \approx 13 \tag{3.12}$$

Thirteen batteries in series give a final output voltage of $48.1V$. The load is attained in (3.13).

$$15kW \cdot 5h = 75kWh \tag{3.13}$$

The capacity required of the battery pack is obtained from the system load and output voltage:

$$\frac{75kWh}{48.1V} = 1559.25Ah \tag{3.14}$$

The capacity per cell is given as 2.6 Ah. The capacity of the battery pack is dependent on the number of batteries in parallel, n_p.

$$n_p = \frac{1559.25}{2.6} = 599.71 \approx 600 \tag{3.15}$$

The battery efficiency coefficient of a lithium-ion battery is expected at $80 - 90\%$ [65]. It is assumed that the battery pack holds an efficiency of 90%. The internal impedance given in the datasheet is set to $\leqslant 180$ mΩ. However, considering section 3.2.2, the internal resistance will be calculated based on the nominal voltage, the efficiency, and the nominal capacity.

$$R_b = V_{nom} \cdot \frac{1 - \eta}{0.2 \cdot Q_{nom}} \tag{3.16}$$

The internal resistance is obtained in (3.17), where it can be noted that the calculated internal resistance of the battery is one order less than the value given in the datasheet.

$$R_b = 48.1V \cdot \frac{1 - 0.9}{0.2 \cdot 1559.25Ah} = 0.0154\Omega \tag{3.17}$$

The size and weight of a BESS are important factors within several areas of use. For a battery system in an electric vehicle, the size and weight are significant for obvious reasons such as the total vehicle volume, speed, as well as the efficiency [66]. For a PV - BESS installation, the battery pack is usually placed in a temperature-controlled room within the residential/office building on which the PVs are placed. In that regard, the battery sizing could be designed with the room area as a basis [67]. The volume of one battery cell is given with a diameter of 19mm and a height of 70.5mm. In the aim of calculating the volume of the entire battery pack, the shape is approximated to a rectangular prism. The width and the length is calculated with relation to n_p and n_s as shown in equation (3.18) and (3.19). It should be noted that as the battery pack consists of two battery models, with the same design, in series. This is taken into consideration when calculating the length of the battery pack in equation (3.19).

$$W = 19mm \cdot 10^{-3} \cdot 600 = 11.4m \tag{3.18}$$

$$L = 19mm \cdot 10^{-3} \cdot 13 \cdot 2 = 0.494m \tag{3.19}$$

Which gives the final volume of the battery package:

$$V = 11.4m \cdot 0.494m \cdot 70.5mm \cdot 10^{-3} = 0.397m^3 \tag{3.20}$$

In the volume calculations of the battery pack, it can be noted that the shape of the battery pack is not optimal with the short height and long width. Therefore, the battery cells should, in practice, be stacked and piled optimally. Multiplying the number of batteries in series of both battery models with the number of batteries in parallel gives the final number of battery cells of 15600. The manufacturer's specification [68] characterizes one

battery with the weight 45.5 grams. This gives the final weight of the battery pack of:

$$45.5g \cdot 15600 = 709.8kg \tag{3.21}$$

3.4 Battery System Implementation in Simulink

All the retrieved values are collected in table 3.1 and implemented in the Simulink battery model. The data regarding voltage, current, and capacity levels were retrieved from the datasheet [64]. From there, the voltages were multiplied with n_s, while the capacity and current values were multiplied with n_p as described above. The values in table 3.1, as well as the discharge curves included in this section, is the resulting characteristics of one battery model. As previously noted, the battery pack used further in this thesis connects two identical battery models in series. Consequently, the current and capacity values are the same, while the voltage over the battery system is twice the size of the voltages in this section.

Table 3.1: Battery Block Parameters

Parameter	Value
Nominal Voltage (V)	48.1
Rated Capacity (Ah)	1559.25
Cut-off Voltage (V)	39
Fully Charged Voltage (V)	54.6
Nominal Discharge Current (A)	312
Internal Resistance (Ohms)	0.0154
Capacity at Nominal Voltage (Ah)	1560
Exponential Zone Voltage (V)	51.86
Exponential Zone Capacity (Ah)	76.61

Figure 3.2 illustrates the nominal discharge characteristic curve of the battery using the model values from Table 3.1. The nominal discharge current is given at $312A$ from the manufacturer's datasheet [64]. The yellow section of the graph represents the exponential

voltage drop when the battery is charged. This section lasts from $t = 0h$ to $t = 0.23h$ which lasts for 13.8 minutes. The second zone is the area which represents the charge that can be extracted from the battery until the voltage is below the nominal voltage. The nominal voltage can be retrieved from table 3.1 as the nominal voltage of one cell multiplied with number of cells in series of one battery model, $48.1V$. After the second section, when the discharge curve reaches $48.1V$, the voltage experience a rapid drop. This section represents the total discharge of the battery to the final time of 5 hours.

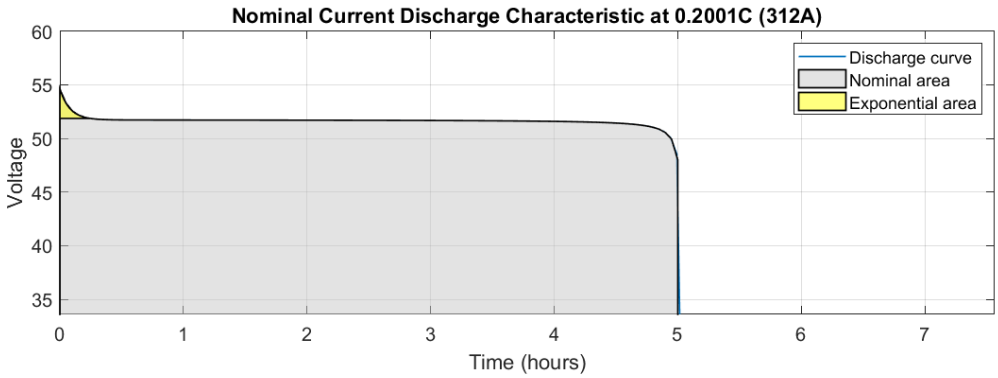

Figure 3.2: The nominal discharge curve of the battery.

The discharge curves for specified discharge currents are shown in figure 3.3. The discharge currents have been decided based on the battery features. The lowest current of 312A is the nominal discharge curve from figure 3.2 and the largest current of 780A is the rapid charge current as retrieved from the datasheet multiplied with n_p. The comparison of figure 3.2 and 3.3 shows that the lower discharge currents lead to a larger nominal area of operation, as assumed. The values written above the graph are respectively the nominal voltage, the internal resistance as well as the polarization voltage (K), the exponential zone voltage (A) and the exponential capacity (B) as previously explained in section 3.2.

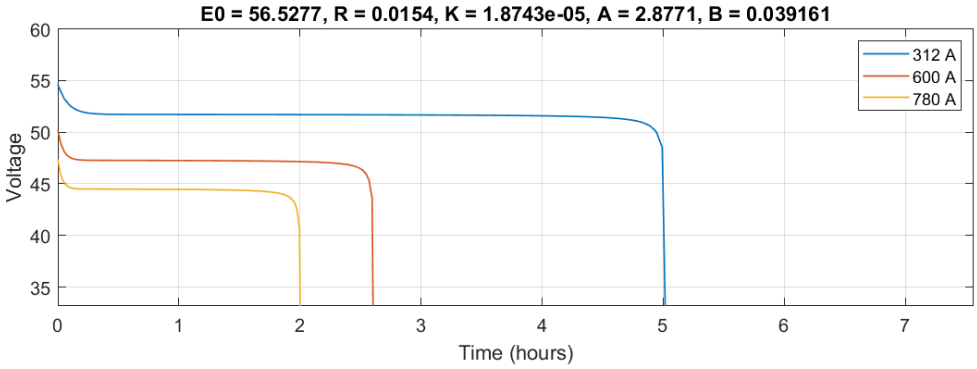

Figure 3.3: Discharge curves for three different discharge currents

Chapter 4

DC-DC Converter

This chapter will present the DC-DC converter technology used further in the thesis to obtain the desired results. The model includes a DC-DC converter to step up the voltage from the battery voltage to a voltage suitable for feeding a voltage source converter. Consequently, the topology and behavior of the converter in this chapter focus on a boost topology. The topology, characteristics, and derivation of model components are presented in section 4.1. In the simulation process, an average model is used. The average model is explained and illustrated in section 4.2. Further, the converter control is described. Section 4.3 describes the roles of both inner current control and outer voltage control, as well as a thorough presentation of the current and voltage PI regulators.

The DC-DC converter holds a significant role in the scope of this thesis. The converter steps up the voltage from the battery system to the voltage source converter. The DC-DC converter is in the computational simulations designed in an average model. The converter controls the current and the voltage by a control strategy based on PI regulators.

4.1 Boost Converter Topology

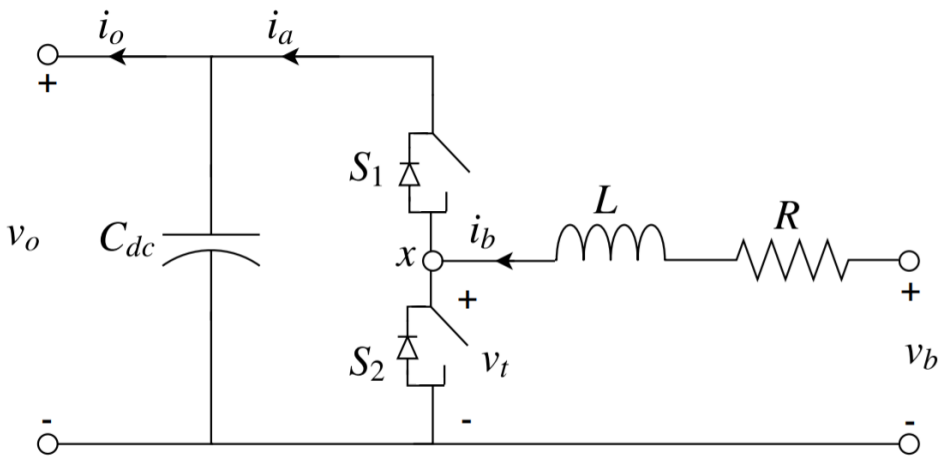

Figure 4.1: Boost converter topology.

Figure 4.1 shows a boost converter, where the switches are operated in a reversed biased fashion. Hence, when S_1 is on, S_2 is off and vice versa. In binary form, the open switch is denoted as $S = 0$ and the closed switch, when the switch is on, is denoted as $S = 1$.

$$\text{Case 1} \begin{cases} S_1 = 1 : close \\ S_2 = 0 : open \end{cases} \tag{4.1}$$

$$\text{Case 2} \begin{cases} S_1 = 0 : open \\ S_2 = 1 : close \end{cases} \tag{4.2}$$

When S_2 is on, the input supplies the inductor with energy. When S_1 is on, the converter output receives the input energy and the inductor energy. In continuous-conduction mode, the steady state time integral of the inductor voltage over one period must be zero, which gives the following expression of the voltages, where t_{on} is the time where S_1 is closed and t_{off} is the time where S_1 is open during one period [69]:

$$v_b t_{on} + (v_b - v_o) t_{off} = 0 \tag{4.3}$$

Equation (4.3) can be rewritten as in equation (4.4) when both sides are divided by the switching period T_s.

$$\frac{v_o}{v_b} = \frac{T_s}{t_{off}} = \frac{1}{1-D} \tag{4.4}$$

Where D denotes the duty cycle of the converter. The fraction $\frac{V_{out}}{V_{in}}$ can be expressed as a gain, g to simplify the duty cycle equation at nominal operation.

$$D = \frac{g-1}{g} \tag{4.5}$$

The circuit can be assumed to be lossless, giving P_b = P_o. The nominal converter current in the high voltage and low voltage side is expressed as in (4.6) and (4.7), respectively.

$$i_o = \frac{P_b}{V_{out}} \tag{4.6}$$

$$i_b = \frac{P_b}{V_{in}} \tag{4.7}$$

The switching period, T_s, is expressed in equation (4.8), where f_{sw} is the switching frequency.

$$T_s = \frac{1}{f_{sw}} \tag{4.8}$$

The inductor current ripple of the boost converter is set to 4%, which gives the value of α as 0.04. This enables the calculation of the current ripple:

$$\Delta I = \alpha \cdot i_b \tag{4.9}$$

By the edge of continuous conduction, the inductor current at boundary level i_{LB} is obtained as in equation (4.10).

$$i_{LB} = \frac{1}{2} i_{l,peak} = \frac{1}{2} \frac{v_b}{L} t_{on} = \frac{T_s v_o}{2L} D(1-D) \tag{4.10}$$

Rewriting the last formulation enables the expression for the inductor:

$$L = \frac{T_s v_o}{2 i_{LB}} \cdot D(1 - D) \tag{4.11}$$

The resistor, R, from figure 4.1 is obtained as in (4.12). The value represents losses in the DC-DC converter from the copper resistivity and switching losses. The rate L/R of the inductor with losses is the circuit's time constant. With the value of R in equation (4.12), the step response of the current through the inductor should experience a smooth behavior, and facilitate the voltage control.

$$R = \frac{v_b^2}{P_b} \cdot 0.005 \tag{4.12}$$

The non-ideal DC voltage ripple of the offset is set to 5%, which enables the calculation of ΔV:

$$\Delta V_o = \alpha_v \cdot v_o \tag{4.13}$$

The capacitance can be calculated on the premise that all the ripple current component of S_1 flows through the capacitor C_{dc}. The peak to peak voltage ripple is given as:

$$\Delta V_o = \frac{\Delta Q}{C_{dc}} = \frac{I_o D T_s}{C_{dc}} \tag{4.14}$$

Using the assumption of constant output current gives the expression in equation (4.14).

$$\Delta V_o = \frac{V_o}{R} \frac{D T_s}{C_{dc}} \tag{4.15}$$

This leads to the final expression of the capacitance as:

$$C_{dc} = \frac{v_o \cdot D \cdot T_s}{\Delta V \cdot R} \tag{4.16}$$

4.2 Average Converter Model

The digital platform based real-time simulation of boost converters is an acknowledged concept in the field of power electronics. Real-time simulations are necessary to get a proper analysis of the converter operation in a complex power electronic model [70]. In the simulation of boost converters, there are mainly two alternatives: a switching model or an average model. This thesis uses an average model to design the converter. The average model causes for less complexity. Further, the simulation time domain is faster of the grid-connected average converters, without losing data from the converter dynamics or accuracy [71; 72]. In the average model, the voltage over the switches or the current through the switches are averaged over one switching period of the model, and the power electronic converter is simulated [70; 73]. The average model ensures the converter operation and simultaneously obeys the specifications from the user. The model is not suitable if the objective of the analysis is to evaluate the switching frequency ripple, as this is not included in the model [74].

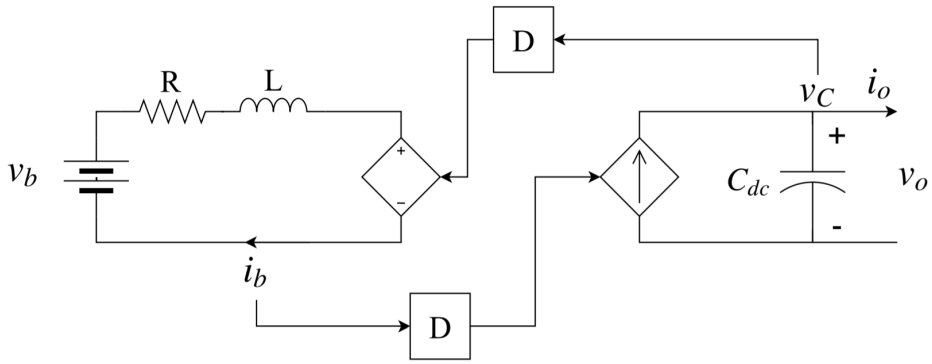

Figure 4.2: Boost converter average model.

The model is illustrated in the conceptual scheme in figure 4.2. In the model the voltage over S_2 (see figure 4.1) and the current through S_1 are averaged over one switching period T_S. S_2 is on during the time DT_s and S_1 is on during the period $(1 - D)T_s$.

4.3 Converter Control

4.3.1 Inner Current Control Loop

The inner current loop gives a fast current response. The control is based on a reference current input, i_{ref}. The controller performs a reference tracking of the current, which ensures that the actual current is approximately equal to the reference current. The per-unit (pu) system is used.

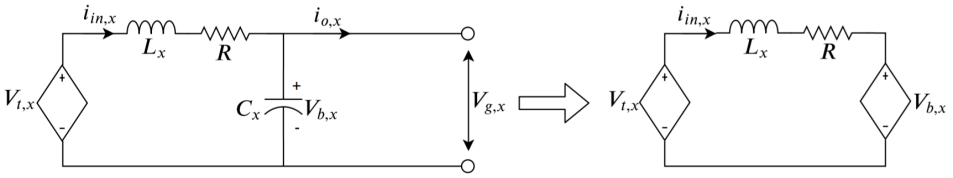

Figure 4.3: Conceptual equivalent circuit of the the inner current control loop.

Figure 4.3 illustrates the inner current loop in an equivalent circuit in a conceptual matter, where the controllable units are clarified. x represents the terminal denoted in figure 4.1. $V_{t,x}$ is the terminal voltage, $i_{in,x}$ is the inner current, $V_{o,x}$ is the voltage out of the inner loop and $V_{g,x}$ is the grid voltage. The circuit elements L_x and R represents the line impedance, and C_x is the parallel capacitance. The resulting control figure to the right shows the inner loop. The resulting KCL and KVL representation of the system is shown in equations (4.17) and (4.18) [75].

$$i_{inx} = C_x \frac{d}{dt} V_{b,x} + i_{o,x} \tag{4.17}$$

$$V_{t,x} = L_x \frac{d}{dt} i_{in,x} + R i_{in,x} + V_{b,x} \tag{4.18}$$

4.3.2 Outer Voltage Control Loop

The outer voltage loop ensures that the voltage is equal to the reference voltage and that any transients are overcome in the fastest feasible time. Figure 4.4 shows the conceptual

equivalent circuit of the outer voltage loop control, with the same denotations as used in section 4.3.1.

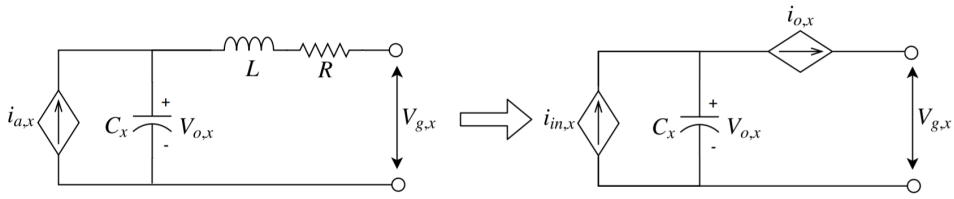

Figure 4.4: Conceptual per phase equivalent circuit of the the outer voltage control loop

The resulting circuit to the right of figure 4.4 shows the outer voltage control where $i_{o,x}$ is based on the load or the grid supply. The resulting KCL representation of the system is shown in equation (4.19).

$$i_{in,x} = C_x \frac{d}{dt} V_{o,x} + i_{o,x} \tag{4.19}$$

4.3.3 Proportional Integral Regulator

The Proportional Integral (PI) regulator is widely used in the industry. This is mainly due to the reduced number of parameters that need to be tuned. PI controllers can provide control signals proportional to the error between the actual output and the reference signal with proportional action. Further, PI regulators can provide control signals to the integral of the error with integral action. With a step reference signal, the integral action of the PI controller enables the elimination of steady-state error of the response to anticipate output changes [28]. Figure 4.5 illustrates the block diagram of a standard PI controller in the Laplace domain. The disturbance is denoted as D in the figure. The further description of a PI controller is with reference to [76]. PI regulators are used in both the current and voltage control for the DC-DC converter.

The equations (4.20) and (4.21) describe the behaviour of a PI controller [76].

$$\dot{\gamma} = y_{ref} - y \tag{4.20}$$

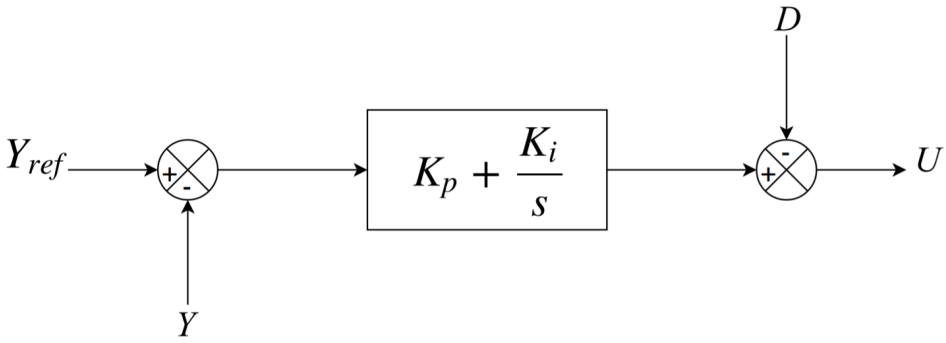

Figure 4.5: Standard block diagram for a PI controller in the Laplace domain.

$$u = K_p(y_{ref} - y) + K_i\gamma_l - d \tag{4.21}$$

Where y_{ref} is the reference value of the system, y denotes the output of the system, u is the controller output, d is the term for decoupling, and K_p and K_i are the proportional and integral gains. The PI controller has the additional state γ_l, l denotes the different PI loops. Equations (4.20) and (4.21) can be represented in the Laplace domain as in (4.22).

$$U = (K_p + \frac{K_i}{s})(Y_{ref} - Y) - D \tag{4.22}$$

When designing a PI controller, the system should first be represented in its standard form, as shown in equation (4.23).

$$H(s) = \frac{b}{s} \tag{4.23}$$

Where b is the plant parameter. This allows for a representation of a closed loop characteristic:

$$A(s) = s^2 + K_p b_s + bK_i \tag{4.24}$$

The standard second order equation is:

$$s^2 + 2\rho\omega_0 s + \omega_0^2 \tag{4.25}$$

Where ρ represents the damping ratio and ω_0 denotes the response speed. When combining (4.24) and (4.25), the controller gains will be set to:

$$K_p = \frac{2\rho\omega_0}{b} \tag{4.26}$$

$$K_i = \frac{\omega_0^2}{b} \tag{4.27}$$

4.3.3.1 PI Current Controller

In the boost converter topology in figure 4.1, the battery voltage expression is:

$$v_b = Ri_b + \frac{Ldi_b}{dt} + v_t \tag{4.28}$$

From following the topology in 4.1, v_t will equal v_o when S_1 is closed. When S_1 is open, v_t will be 0 when S_1 is open. This gives the expression of v_t as in equation (4.29).

$$v_t = v_o \cdot S_1 \tag{4.29}$$

In equation (4.28), the controlled link is $v_o S_1$, which further is expressed as μ.

$$\frac{Ldi_b}{dt} = v_b - Ri_b - \mu \tag{4.30}$$

The losses of Ri_b can be neglected when tuning the PI regulator.

$$K_p(i_b^* - i_b) + K_i \int_0^t (i_b^* - i_b)dt = v_b - \mu \tag{4.31}$$

Here, i_b^* is the reference current of the battery. The difference from the reference current to the actual current is the system error, e.

$$\mu = -(K_p e + K_i \int_0^t edt) + v_b \tag{4.32}$$

Expanding μ gives a further expression of the average duty value (D).

$$D = [-(K_p e + K_i \int_0^t e dt) + v_b] \cdot \frac{1}{v_o} \tag{4.33}$$

To simplify the expression, the output voltage can be approximated at its nominal value $\overline{v_o}$:

$$D = [-(K_p e + K_i \int_0^t e dt) + v_b] \cdot \frac{1}{\overline{v_o}} \tag{4.34}$$

The analog sensors of the current controller are denoted as T_a and the time constant of the controller is expressed as in equation (4.35)

$$\tau = \frac{L}{\omega_b R} \tag{4.35}$$

Where ω_b is the base angular frequency, and L and R are the inductance and resistance, respectively. From this, the current proportional gain K_p and the current integral gain, K_i can be calculated.

$$K_p = \frac{L}{2\omega_b T_a} \tag{4.36}$$

$$K_i = \frac{K_p}{\tau} \tag{4.37}$$

4.3.3.2 PI Voltage Controller

Following the alternating current i_a in figure 4.1, it can be observed that the current equals i_b when S_1 is on, and that the current is 0 when S_2 is off. Consequently, i_a can be expressed as:

$$i_a = i_b \cdot S_1 \tag{4.38}$$

The current dynamics can be written as in equation (4.39).

$$i_a - i_o = C_{dc} \frac{dv_o}{dt} \tag{4.39}$$

i_a is the controllable signal and is denoted as μ_v. Denoting the deviation between the reference voltage and v_o as the error e_v, the expression of μ_v becomes:

$$\mu_v = K_{pv} \cdot e_v + K_{iv} \int_0^t edt + i_o \tag{4.40}$$

In the voltage control loop design, it is possible to use an approximation model of the current controlled loop. This approximation uses a first-order model with a time constant of T_e. The time constant T_e is calculated as in equation (4.41) [77].

$$T_e = 2 \cdot T_a \tag{4.41}$$

Where, T_a is the time constant used in the current controller for i_b described above. The proportional characteristics between i_a and i_b allow the hierarchical control strategy. The dynamic of the system modeled is given in equation (4.39). The PI voltage controller is tuned by applying symmetrical optimum to the per unit system in accordance with reference [77]. When applying symmetrical optimum to the outer system, the lead compensator of the open loop transfer function is as in equation (4.42).

$$H_{ol}(s) = K_p \frac{(s+z)}{s} \frac{1}{s+p} \frac{b}{s} \tag{4.42}$$

The PI controller can be expressed as in equation (4.43)

$$PI(s) = K_{pv} + \frac{K_{iv}}{s} = \frac{sK_{pv} + K_{iv}}{s} = K \frac{s+z}{s} \tag{4.43}$$

Where K_{pv} is the voltage proportional gain and K_{iv} is the voltage integral gain. In the simplification process, K_{pv} is denoted as K and K_{iv} is denoted as Kz. Finding the values of the controller gains, b is represented in (4.44) and p is represented in (4.45), where T_e is retrieved from equation (4.41).

$$b = \frac{\omega_b}{C_{pu}} \tag{4.44}$$

$$p = \frac{1}{T_e} \tag{4.45}$$

The constant z is calculated as the fraction between p and a gain α, as in equation (4.46). The gain, α, is an input which compiles if it obtains a value higher than 1. In this project, as in [77], α is set to 6.

$$z = \frac{p}{\alpha} \tag{4.46}$$

ω_m is the geometric mean of the zero and pole, and is calculated as follows:

$$\omega_m = \sqrt{zp} \tag{4.47}$$

Further, the voltage proportional gain is obtained as in equation (4.48), this leads to (4.49), which gives the voltage integral gain.

$$K_{pv} = \frac{\omega_m \cdot C_{pu}}{\omega_b} \tag{4.48}$$

$$K_{iv} = z \cdot K_{pv} \tag{4.49}$$

Chapter 5

Power Hardware in the Loop

This chapter will present the testing method power hardware in the loop (PHIL). Section 5.1 explains the conceptual basis of the hardware in the loop strategy, and how power hardware in the loop is a beneficial extension of this strategy for the purpose of this thesis. Moreover, section 5.2 presents how the testing technology can be applied in other industries and purposes. The PHIL structure used further is then presented in section 5.3, before section 5.4 gives the theoretical discretization algorithm used to enable the model to emulate the energy storage system for testing.

Results based on simulations have the risk of differing between different programs, mathematical models, and the complexity of the model. On the other hand, laboratory experiments usually come at a high cost and require a long developing period. Therefore, the PHIL technique is in this case used to test the system dynamics and acquire realistic results [78]. Hardware in the loop simulation is a method of simulating a model based on a real-time simulation where the physical inputs and outputs are connected to the designated components. Under controlled circumstances, this enables tests with realistic results. The purpose of the simulation model is to attain realistic behavior. The accuracy requirements must be assessed individually for each application it is intended for.

5.1 PHIL Concept

The term HIL (Hardware In the Loop) or CIL (Controller in the loop) is based on one simulation which combines testing of both hardware and software. The hardware is connected to the model loop, where the software modeled controls the control strategy of the process. This allows for an analysis of the system under realistic conditions. A dynamic and structured HIL test setup allows one to complete standardized tests in the development process and after completion. The HIL framework consists of a control unit, a system model, and inputs and outputs. The testing usually occurs with low power signal interfaces. However, in some cases, high voltage and high current interfaces are required in HIL. In that case, it is required with high voltage and high current, high frequency and high accuracy amplifiers. This is necessary to interface with the controllers and protection systems. Consequently, the power rating is relatively low, and the amplifier load cannot influence the simulation. To solve these issues, PHIL simulation is introduced. PHIL is the integrated simulation of a complete system. In the system, one part is simulated numerically, while the other is tested using physical devices. Figure 5.1 illustrates the PHIL concept. Here, the amplifier has the capability to feed the device under the test, as well as to absorb power generated by the devices. In the PHIL tests, the global simulation is influenced by the amplifier loads [79].

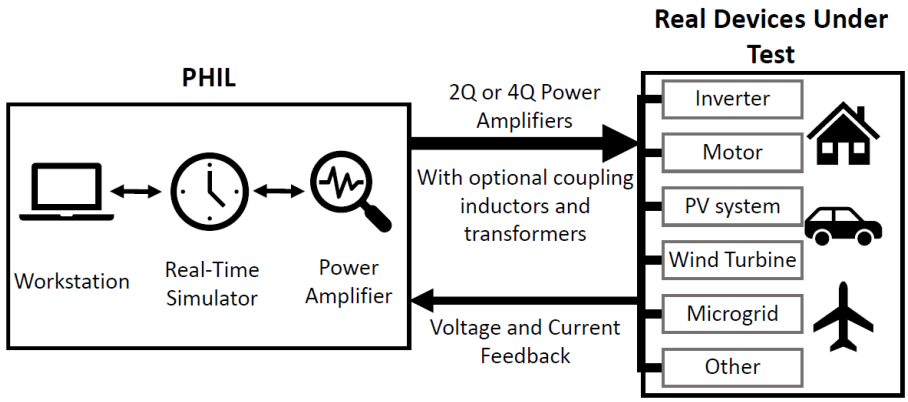

Figure 5.1: Power hardware in the loop concept

PHIL simulators can be used to simulate communication networks, as well as the in-

teraction with hardware. This enables the integration of multiple protocols and systems into one single system. In the PHIL system aspects, the emulation of a microgrid and loads can be modeled to analyze the subsystem interaction. In the system, each subsystem can be modeled in three ways. Either, the subsystem is the actual system operating under nominal ratings. Secondly, the subsystem can be scaled down to an analog model. Lastly, the subsystem can be an emulated PHIL model. In this regard, the power tests can be conducted without detailed models, which leads to a possibility of managing tests too risky to do with the actual physical system [79].

5.2 HIL and PHIL Applications

HIL systems are growing more popular over a variety of fields, among others due to the growing complexity within software-based control systems [80]. HIL is among other fields actively used in the field of unmanned aerial vehicle (UAV). The aerospace field was the first to use HIL testing to analyze safety-critical software systems with the objectives of developing safer systems quicker while simultaneously reducing costs [81]. Reference [82] designed a HIL for autopilot based on X-plane. Reference [83] analyzed the HIL use for the UAV controlled system. Reference [83] and [84] based their UAV HIL models on MATLAB/Simulink. The HIL testing technology is also used in the automotive industry. Reference [85] reports that 90% of the faults found in traditional test drives were found significantly quicker and cheaper with HIL simulations in the automotive industry.

PHIL testing can be applied in numerous fields. In grid application, it can be used for grid emulation, PV-inverter emulation, wind-generator emulation as well as grid inverter emulation. Reference [86] tested a 500kW photovoltaic array inverter. The emulation of the PV array was conducted with the use of a real-time simulator with a DC amplifier, and an AC amplifier was used to emulate the power grid. In [87], an equivalent circuit model of pressure retarded osmosis is used to develop a PHIL emulator to represent an osmotic power plant with the use of a real-time simulator. Reference [88] uses hardware in the loop testing to verify algorithms regarding the output characteristics of a wind turbine.

In microgrids, it can among others be used to emulate the motor or generator used, the drive inverter and the frequency inverter. Reference [89] evaluates two interface designs for PHIL experiments. This is used to define a design procedure based on optimization for PHIL testing of electrical drives. An FPGA based real-time simulation system was tested according to the PHIL method in [90]. The testing object used was a nonlinear permanent magnet synchronous machine, and the paper takes on its qualification for PHIL emulation systems. In [91], a modular multiphase multilevel converter is presented for the usage in PHIL emulation systems.

Further, the aerospace and military industry can, for instance, use the PHIL testing structure for the emulation of a 400 Hz aerospace device. Reference [92] describes a HIL simulator for the usage in the design and testing of fault tolerant control and condition monitoring schemes for fluid power systems to be applied in control applications. Results obtained from real-time simulation using HIL for aerospace power systems are presented in [92] with the use of embedded processors and FPGAs in the computing infrastructure. The applications within the automotive industry can use PHIL testing for the emulation of an electrical drive train, where the battery, drive inverter, and motor can be emulated. Reference [93] presents a supercapacitor driven subway line with a reduced scale PHIL simulation for experimental validations. A subway line is also tested through PHIL in [94] where a traction power substation supplies the subway through a DC energy rail.

5.3 PHIL Structure

The system outline is defined in figure 5.2. The DC-DC converter circuit is included in the real-time simulator (RTS). The converter is based on an average model of a boost converter. It can be observed that the physical voltage source converter sends voltage and current measurements to the RTS, which is the corresponding voltage v_m over the capacitor in the RTS as well as the controlled current i_m of the circuit. The RTS is connected to the real device under testing (DUT), which is a physical three-phase voltage source converter. From there, the measurements of voltage and current are signaled to the RTS. The RTS simulates the energy storage model of the battery pack and bidirectional converter and a

load. As illustrated in the figure, the RTS sends a voltage signal to the physical equipment to a controlled voltage source.

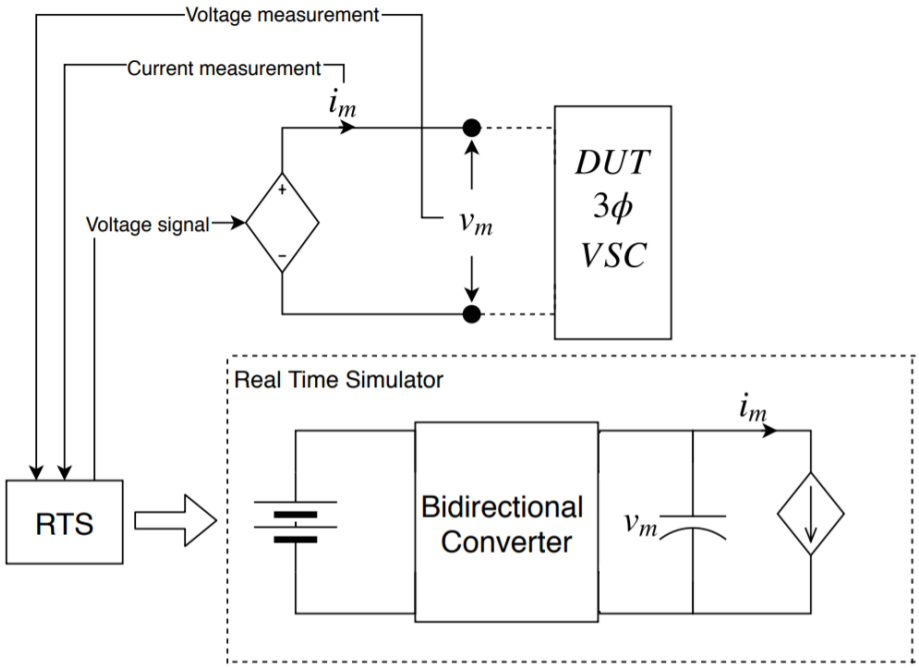

Figure 5.2: Outline of PHIL Structure for emulation of ESS.

5.4 Discretization Algorithm

As illustrated in figure 5.2, a voltage source model is required to send the voltage reference to the controlled voltage source. In order to obtain the voltage model, a discrete model at the capacitor of figure 5.2 is obtained in the following subsection. The discretization aims to model the parallel connection of a controlled current source and the capacitor into its Thevenin equivalent circuit, as represented in figure 5.3. This procedure enables an emulation of the energy storage system up to the controlled current source of the high voltage side of the converter.

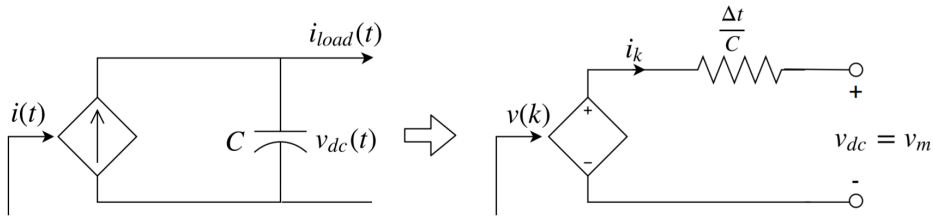

Figure 5.3: Illustration of discretization objective.

From Kirchhoff's current law, the current loop can be described as:

$$C\frac{dv_{dc}(t)}{dt} = i(t) - i_{load}(t) \tag{5.1}$$

Where, i(t) is controllable and $i_{load}(t)$ is the disturbance. The expression can further be represented in the Laplace domain as in equation (5.2).

$$CsV_{DC}(s) = I(s) - I_{load}(s) \tag{5.2}$$

where, $V_{DC}(s), i(s)$ and $i_{load}(s)$ are the same variables as above in the Laplace domain.

The trapezoidal approach of discretizing continuous signals leads to [95]:

$$s = \frac{2(z-1)}{T(z+1)} \tag{5.3}$$

The system in the z-domain is represented as follows:

$$C\frac{2(z-1)}{T(z+1)}V_{dc}(z) = I(z) - I_{load}(z) \tag{5.4}$$

$$2C(z-1)V_{dc}(z) = T(z+1)I(z) - T(z+1)I_{load}(z) \tag{5.5}$$

The trapezoidal approach asserts that a signal multiplied with z equals the signal one sample time ahead. This is implemented in discrete form equation (5.6) and reordered in equation (5.7).

$$v_{dc,k+1} - v_{dc,k} = \frac{T}{2C}(i_{k+1} + i_k) - \frac{T}{2C}(i_{L,k+1} + i_{L,k}) \tag{5.6}$$

$$v_{dc,k+1} = v_{dc,k} + \frac{T}{2C}(i_{k+1} + i_k - i_{L,k+1} - i_{L,k}) \tag{5.7}$$

Using the instant time current gives the following expression in (5.8).

$$v_{dc,k} = v_{dc,k-1} + \frac{T}{2C}(i_k - i_{k-1} - i_{L,k-1} - i_{L,k}) \tag{5.8}$$

The circuit at the right side of figure 5.3 can be obtained from (5.8). Equation (5.8) is used in the computational model to obtain the same signals as the continuous time model. Consequently, it is obtained that $\Delta t = \frac{T}{2}$. The voltage drop is obtained with the measured current i_k and the computed resistor $\Delta t/C$. The output voltage is $v_m = v_{dc,k}$, and the controlled voltage source is calculated with the remaining part of the terms.

Chapter 6

Computational Results

The objective of this chapter is to test the control configurations from the literature review. The chapter will give a good evaluation of the discrete design implemented, as it can be compared to the continuous model. The most extensive part of this thesis, aside from the laboratory work, is the computational results. The resulting developed model consists of a battery model connected to a bidirectional DC-DC converter. To develop the resulting model, a step - by - step methodology was used. First, the battery design was developed and tested, as shown in chapter 3. The bidirectional converter was designed as an average model, and the current and voltage control was implemented as in section 4. This chapter takes on the resulting graphs from the model of a battery pack connected to a bidirectional converter with an implemented current and voltage control. Section 6.1 presents the resulting graphs of the bidirectional converter control with the battery pack. Secondly, the battery model is tested computationally with the system designed according to 3.3. In section 6.3, the discretization algorithm is tested through simulations and compared to the continuous model results. Section 6.4 shows how the implementation of noise affects the resulting output of the model. The chapter ends with a discussion of the computational results.

The simulations are conducted in the MATLAB/Simulink environment. Simulink is a block diagram tool that supports multidomain simulations. The designs are model-based, and there are automatic code generation, continuous test, and verification of the embedded systems. The program includes a graphical editor and customizable block libraries [96].

6.1 DC-DC Converter connected to Battery System

The DC-DC converter is modeled to regulate voltage and current. Table 6.1 lists the parameters of the converter considered during the simulations. During the control, all parameters (except time) are converted into the per unit (pu) system. The DC-DC converter model is created in MATLAB/Simulink as an average model with a current and voltage control. The nominal voltage of the battery pack was $96V$, and the converter was modeled to provide an output voltage of $650V$. The input voltage parameter for the design of the converter is $300V$, which means that the converter can be applied to an extension of both two and three battery packs. This section addresses the current output I_{out} and the voltage output V_{out}. Furthermore, the section includes the current and voltage errors from the controller in the per unit system, to ensure functioning control, which are attained with the use of Proportional Integral (PI) regulators.

Table 6.1: Converter Parameters

Base Parameters	**Actual Value**
Power	20 kVA
Frequency	50 Hz
Switching Frequency	10 kHz
Input Voltage	300 V
Output Voltage	650 V
Nominal Current	33.33 A
Inductance	5.625 mH
Resistance	22.5 mΩ
Capacitance	55.556 μF

Figure 6.1 presents the resulting graphs of a 10 seconds simulation of the model. The uppermost graph takes on the control of the converter. The voltage and current errors are depicted in the per unit system. Both error curves show an initial oscillation before stabilizing at zero. The middle graph presents the current out of the converter, which stabilizes at $12.3A$. The voltage graph at the bottom of V_{out} stabilizes at $650V$, as expected.

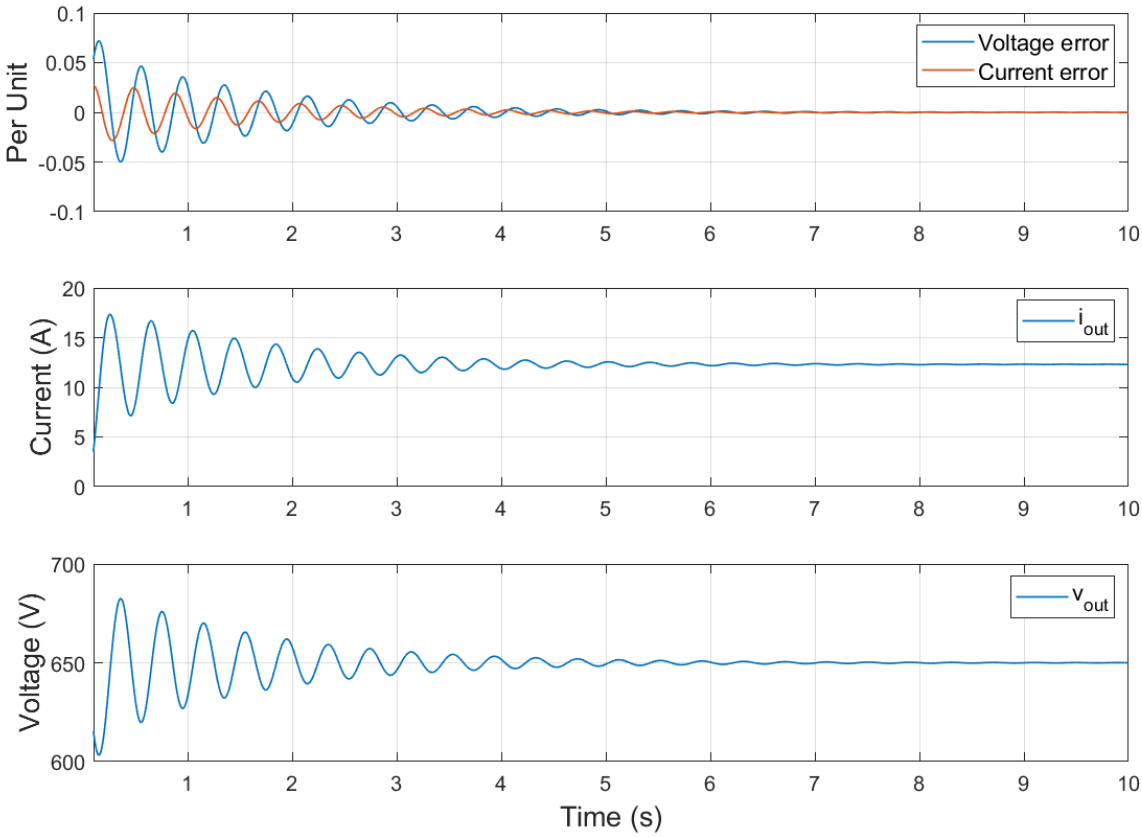

Figure 6.1: Resulting graphs from the bidirectional converter model. The top graph shows the voltage and current error from the controller. The middle graph is the current output and the bottom graph shows the voltage output of the converter.

6.2 Battery Model

The battery system is connected to the low voltage side of the converter. It is computationally modeled with the standard Simulink/Simscape library lithium-ion battery. The design is conducted according to section 3.3.

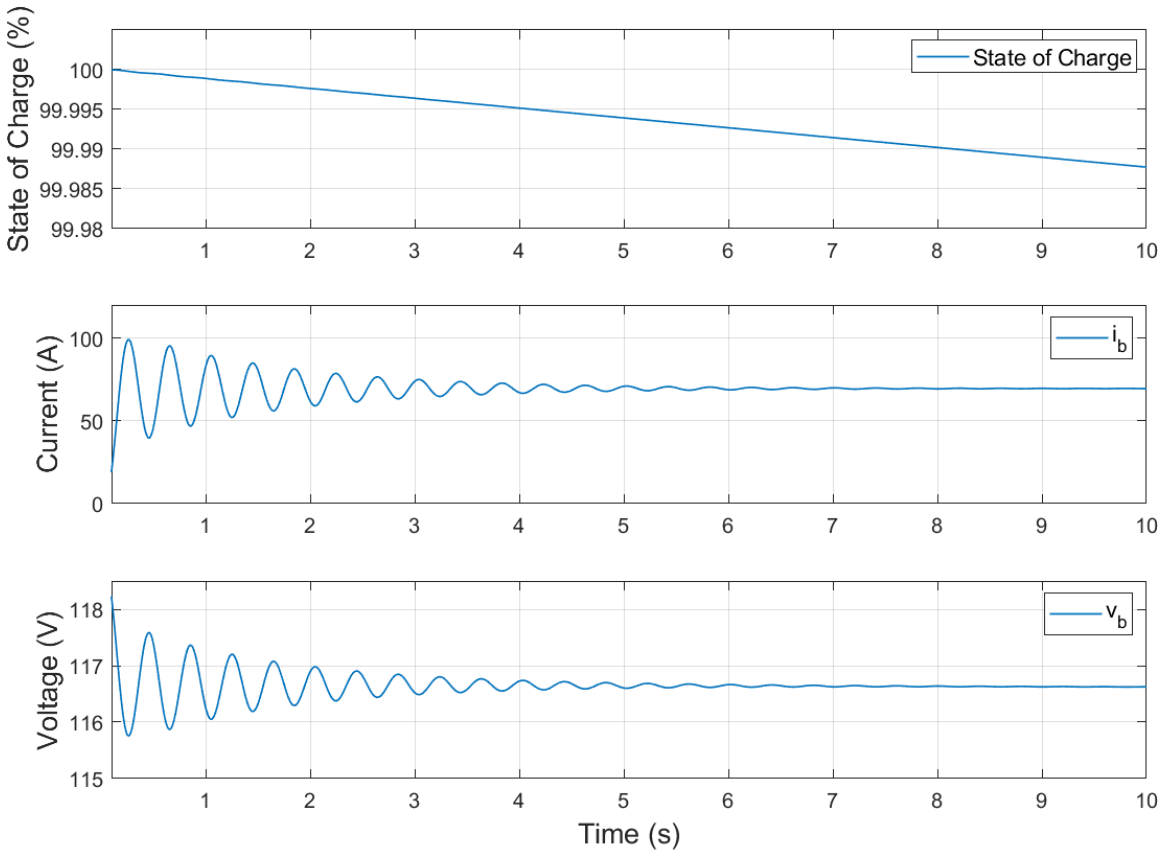

Figure 6.2: Resulting graphs from the discharging battery model. The top graph shows the state of charge, the middle graph is the current out from the battery and the bottom graph shows the voltage over the battery system.

The battery starts with an initial full battery with the SOC of 100%. From there, after 10 seconds, the battery SOC drops to 99.98774 %, which leads to an average decline in charge of $1.226 \cdot 10^{-3}\%$ per second. The battery current i_b stabilizes at 69.5 A, after an oscillating initialization. The battery voltage over the battery system is stabilizing at 116.6 V. Figure 6.3 presents the discharge curve for one of the two batteries in series with the correct value of the discharge current at 69.5 A.

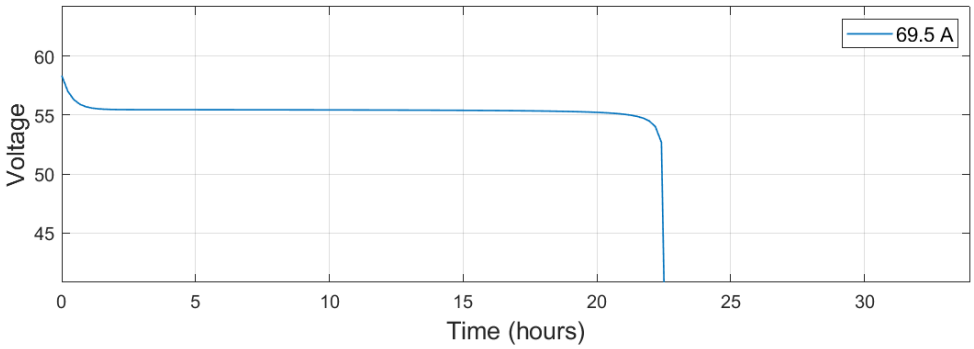

Figure 6.3: Discharge curve with the discharge current observed is the resulting scope.

6.3 Discrete Model

The objective of the discretization was to emulate the continuous model. Therefore, the comparison between the two is best done if both models are scoped in the same graphs. Figure 6.4 presents the continuous model results i_{out} and v_{out} as the green lines, and the discrete signals i_K and v_{DC} as the yellow lines. It can be observed that both the discrete and continuous signals behave identically, which is why the signals from the continuous model are represented with thicker green lines to depict both results. The signals behave similarly to the signals presented in 6.1.

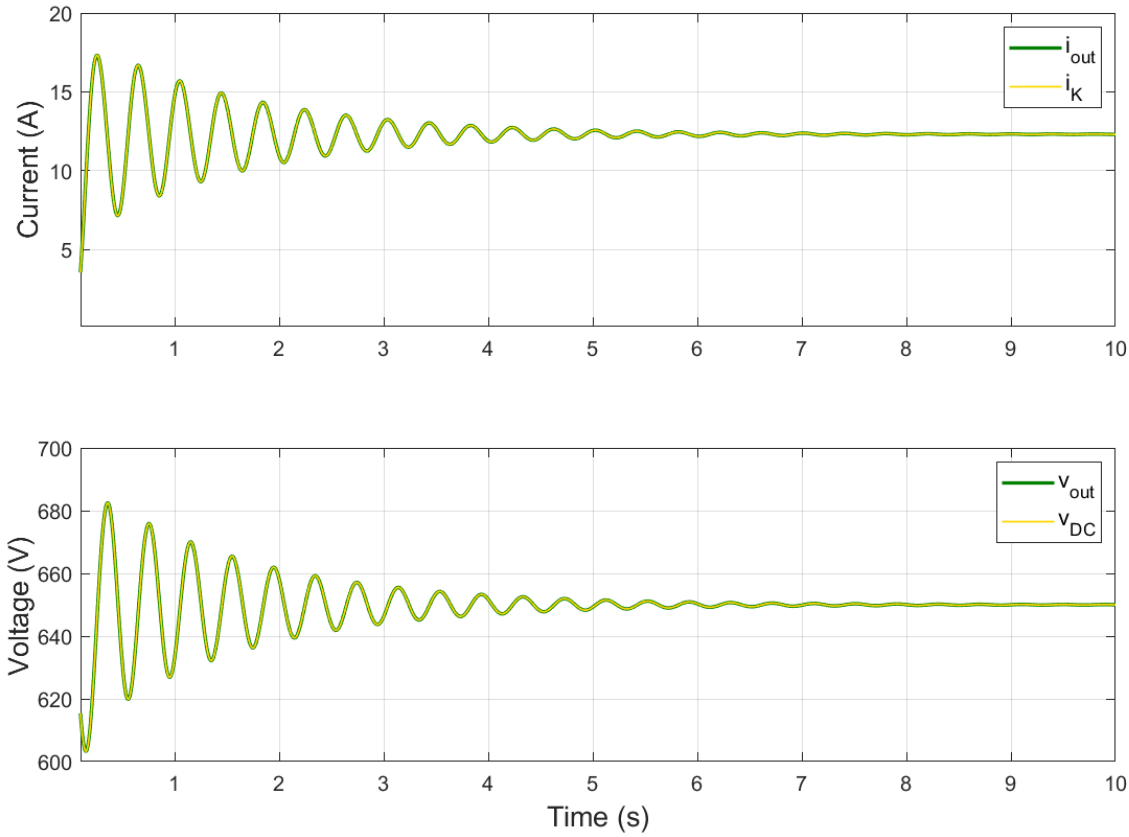

Figure 6.4: The top graph shows the current output i_{out} and the discretized current output i_K. The bottom graph shows the voltage output v_{out} and the discretized voltage output v_{DC} of the converter.

6.4 Implementation of Noise

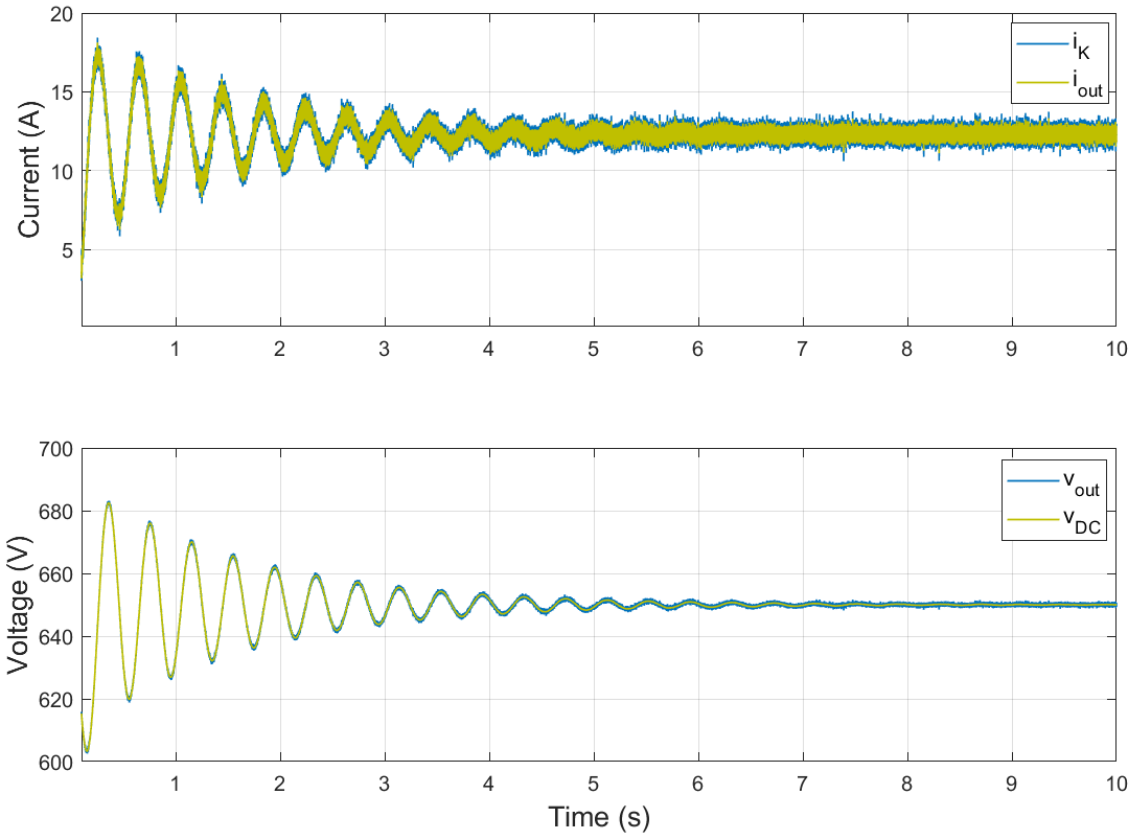

Figure 6.5: The top graph shows the current output i_{out} and the discretized current output i_K with the inclusion of noise. The bottom graph shows the voltage output v_{out} and the discretized voltage output v_{DC} of the converter with the inclusion of noise.

To ensure realistic simulation results in view of the experimental validation, noise was added to the computational model in the output voltage and current. The noise was modeled in Simulink as a random number, changing by the rate of the switching frequency given in table 6.1. The output number of the noise was a normally distributed random signal. The variance of the noise was attained from tests at the Norwegian Smart Grid Laboratory. The voltage variance is set to 0.1150, and the current variance is set to 0.0609. The

top graph of figure 6.5 shows that the voltages of the continuous and discretized model behave similarly, with the initial oscillation before both stabilize at the desired output voltage of $650V$. The currents in figure 6.5 also show corresponding performance with the added noise.

6.5 Discussion of Computational Results

It is clear from section 6.1 that the voltage and current error hold an initial oscillation before stabilizing to zero. This is an effect that is reflected throughout the computational results, where it can be observed an initial oscillation at the same length in all graphs. The converter is modeled to provide an output voltage of 650 V, which is where the voltage of the converter, as well as the discretized signal, are stabilizing. The graphs show the correspondence between the error curves and the current and voltage curves. The output current I_{out} stabilizes at $12.3A$, which is the product of the current at the low voltage side, that is the current out of the battery pack, multiplied with the controlled average duty signal.

The resulting graphs from the battery model are presented in section 6.2. The nominal discharge current is set to 0.52 A times the number of batteries in parallel (600). This leads to the nominal discharge current of 312 A, significantly less than the current through the battery, leading to a slow discharge of the battery. From section 3.4 it can be observed that the discharge currents are all considerably higher than the discharge figure presented in 6.2, which leads to a significantly longer time span of the operation in figure 6.3. Figure 6.6 shows the discharge curve for the first 10 seconds, as the other resulting graphs. The voltage of the battery here operates with a voltage from 58.33 to 58.32, which leads to the total voltage of the two batteries in a range of 116.6 V. The measured voltage stabilizes on 116.6 V as assumed from this analysis.

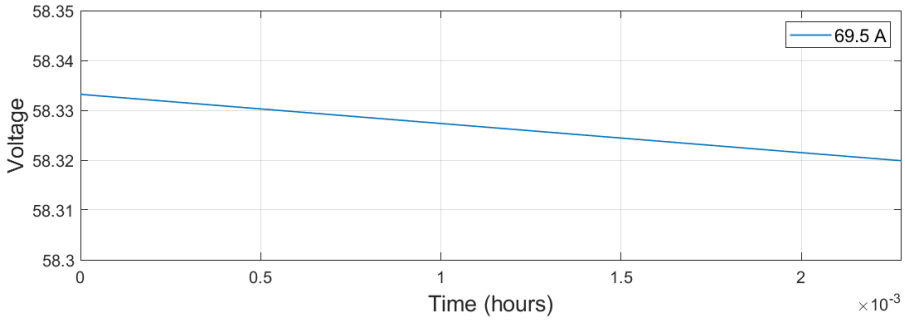

Figure 6.6: Discharge curve with the discharge current observed is the resulting scope.

The battery charging process is not an extensive part of the computational results, but it is included in appendix B. As the battery, in that case, is only connected to a controlled current source without a DC-DC converter nor a control system, the results are bound to be less realistic than the results included in this chapter. However, with the same current rating of the source, it creates a basis for comparisons. This leads to the resulting charging graphs with no oscillating part, and the system stabilizes instantly. The state of charge is increasing with $1.238 \cdot 10^{-3}\%$ per second, while the discharged battery decreases its SOC with $1.226 \cdot 10^{-3}\%$ per second. These values are relatively similar, due to the similar current running through the battery (though in opposite directions). The battery current i_b running through the discharging battery in section 6.2 is not exactly 69.5, which can be the reason why the SOC does not behave inversely proportional.

Section 6.3 shows the comparison of the continuous model versus the discretized model. The resulting graph verifies the discretization algorithm based on the signals matching each other throughout the ten seconds. Noise was added to the signals in section 6.4. This was done to ensure a realistic result to later establish a smooth transition to the physical equipment in the laboratory. The voltage variance of noise was higher than the current noise but caused for a lower percentage of the signal in the case of a high voltage low current model. The simulated model of the energy storage system has a capacitance of $55.556\mu F$, which is a relatively low capacitance. This is designed according to equation 4.30 in section 4.1. However, the capacitor in the physical converter at the laboratory has

a value of $14mF$, which is significantly larger. Additionally, the current step from 1 to 12.3 amperes is relatively big, which leads to a slow response. This makes a high and low frequency oscillation in both the voltages and currents.

Chapter 7

Laboratory Work

This chapter will provide a presentation of the laboratory work conducted to test the theoretical ideas and simulated models. The model uses a PHIL testing strategy, as presented in chapter 5, of a simulated model like the one in chapter 6. The first section introduces the testing site, the laboratory setup, and the physical equipment used to obtain the results. The results are presented in section 7.2, where both the real-time simulation (RTS) and physical sensor signals are included. The current and voltage graphs prove the functionality of the power hardware in the loop testing method. Lastly, the results are discussed and analyzed deeper in section 7.3.

The computational results showed a functioning controller. With the smart grid laboratory facilities of SINTEF and NTNU, the system was tested with the use of physical equipment as well as the simulated model. This chapter presents a functioning emulation of an energy storage system, as well as confirming the functionality of PHIL.

7.1 Laboratory Setup

The Norwegian national smart grid laboratory in Trondheim is built by NTNU and SINTEF. The laboratory is system oriented, and its purpose is to provide a state of the art infrastructure for research and development, verification and testing over various use cases of smart grid application. The laboratory design enables the possibility of integrating RTS and physical power system assets in a PHIL setup with a rating up to 200 kVA, 400 V AC or 700 V DC. The laboratory can be used to test numerous systems such as smart home management systems, multi-terminal HVDC grid connecting offshore wind farms, frequency support from wind turbines, product testing and verification, microgrids and lastly, the use of this thesis, power hardware in the loop.

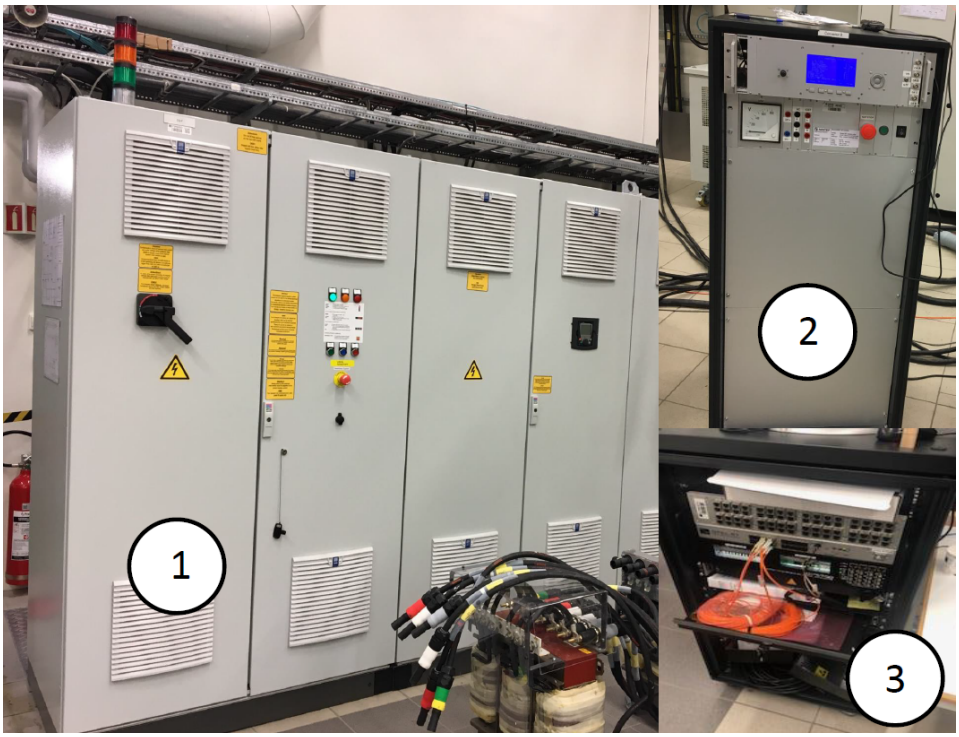

Figure 7.1: Norwegian Smart grid Laboratory. (1): 200kVA Controlled Voltage Source, (2): 60 kVA $3-\phi$ VSC, (3): OPAL-RT.

The laboratory testing was conducted in the Norwegian Smart Grid Laboratory depicted in figure 7.1. The model was implemented with an OPAL - RT simulator with a

sampling time $Ts = 100\mu$s, which signaled the physical laboratory equipment.

7.1.1 Controlled Voltage Source

Figure 7.2 shows the controlled voltage source used in the laboratory setup. It is a 200kVA digital amplifier. It is of the model COMPISO System Unit 200-1GAMP6. The amplifier works as a turnkey PHIL solution for electrical power system testing. The unit includes six four-quadrant digital power amplifiers that can operate DC up to 5 kHz full span output voltage. The system provides the power path, safety infrastructure, and software applications to the configuration of running tests [97].

Figure 7.2: 200kVA Controlled Voltage Source

7.1.2 Voltage Source Converter

The voltage source converter used in the laboratory setup is presented in figure 7.3. The converter is rated at 60 kVA AC / DC. It includes an LCL filter, a contactor, and a charging circuit.

Figure 7.3: 60 kVA $3-\phi$ VSC

7.1.3 Real Time Simulator

In the testing, the Opal-RT 5700 in figure 7.4 is used. This is a complete simulation system. The OP5700 includes a target computer, a reconfigurable field-programmable gate array (FPGA), signal conditioning for up to 256 I/O lines and 16 high-speed fiber-optic small form-factor pluggable ports. The AC input is rated to 100-240 V, and 60-50 Hz [98].

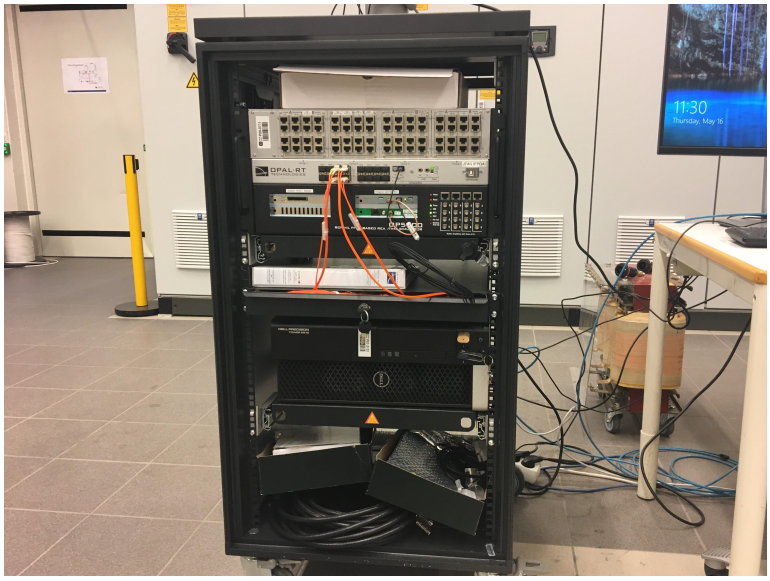

Figure 7.4: OPAL-RT.

7.2 Laboratory Results

This section presents the laboratory results of the output voltage and current for both the physical measurements, as well as the one included in the discretized simulation model. The objective of this section is to obtain an emulation of the battery and the DC-DC converter in a real-time simulation connected with a physical voltage source converter and a controlled voltage source through the power hardware in the loop testing strategy. The included results presented are a collection of logged data from the system under different conditions: constant current, a slight increase of current, rapid increase of current and rapid decreasing of current. The change in current was physically increased and decreased by turning a rotary control knob. The degree of rotation corresponded with the current output, while the speed of rotation corresponded with the current change velocity, as the testing occurred in real-time. The time periods between the data logs are averaged with a dotted grey line.

7.2.1 Current Results

Figure 7.5 presents the resulting current from the laboratory tests. This graph contains two different measurements. The black line represents the current i_k, the signal from the real-time simulator, which represents the simulation. The gray dashed line represents a constant estimated average between data logs. The blue, green, and orange lines are the output current data logs from the physical laboratory equipment, i_{out}. The data logs are explained below.

1. **The first section** is logged from t = 321 s to t = 347 s. It is in figure 7.5 illustrated as the blue area. The section is initialized with 10 seconds of constant current. From t = 331 s to t = 347 s the current ramp has an average increase of 0.1 amperes per second.

2. **The second section** is logged from t = 374 s to t = 397 s. This area is in figure 7.5 the green area. The section starts with a 16-second current ramp. The current ramp has an average increase of 0.13 amperes per second. From there, the current remains unchanged for 7 seconds.

3. **The third section** is logged from t = 479 s to t = 493 s. In figure 7.5, the section is represented as the decreasing orange area. From t = 479 s to t = 489 s the decreasing current ramp has an average decrease of 0.36 amperes per second. The graph ends with an unchanged current in the third section of 5 seconds.

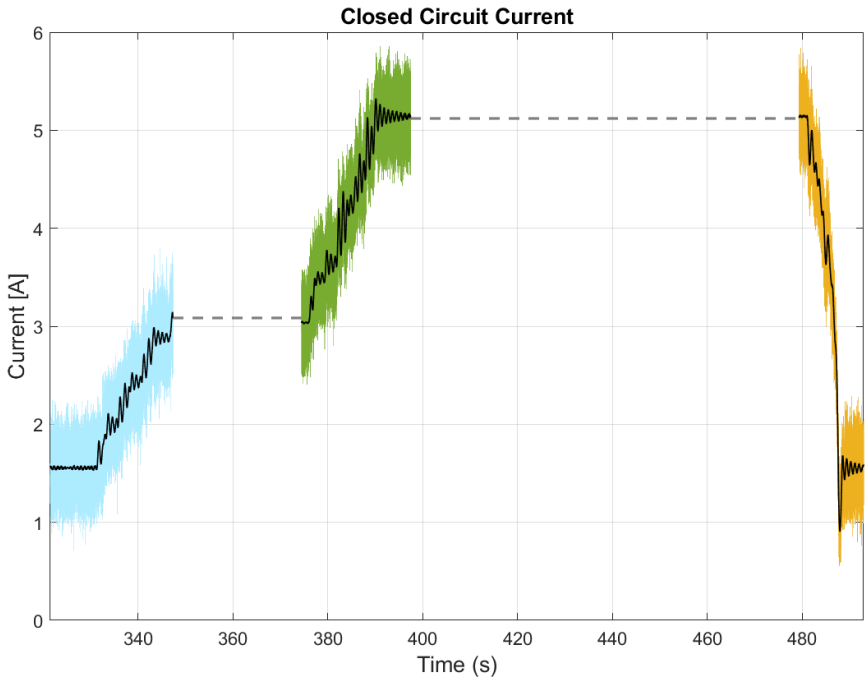

Figure 7.5: Current output i_{out} from the continuous model as the blue, green and orange line and i_k from the physical measurement as the black line.

7.2.2 Voltage Results

Figure 7.6 shows the voltage output graph from the laboratory tests. The voltage output v_{DC} from the continuous model and v_{out} from the physical equipment are perfectly correlated. Consequently, it looks like only one value is measured at each time, even though in fact, both the voltage from the simulation model and the value from the physical equipment test is included. The voltage is kept around the value of 650, but with some apparent noise. The blue, green, and orange lines represent v_{out} and v_{DC} at the three data logs explained below.

1. **The first section** is logged from t = 321 s to t = 347 s. It is in figure 7.6 illustrated as the blue area. The amplitude of the noise in the first section is largest at the value of 649.751 V at t = 336 s, with the amplitude 0.249.

2. **The second section** is logged from t = 374 s to t = 397 s. This area is in figure 7.6 represented as the green area. The voltage deviates most from 650 V at t = 388 s at the value of 649.462 V. This leads to an amplitude of 0.538.

3. **The third section** is logged from t = 479 s to t = 493 s. In figure 7.6, the section is illustrated as the orange area. The section has a clear amplitude at its most deviating point in t = 488 s with the value of 650.843 V, which gives the largest amplitude of 0.843.

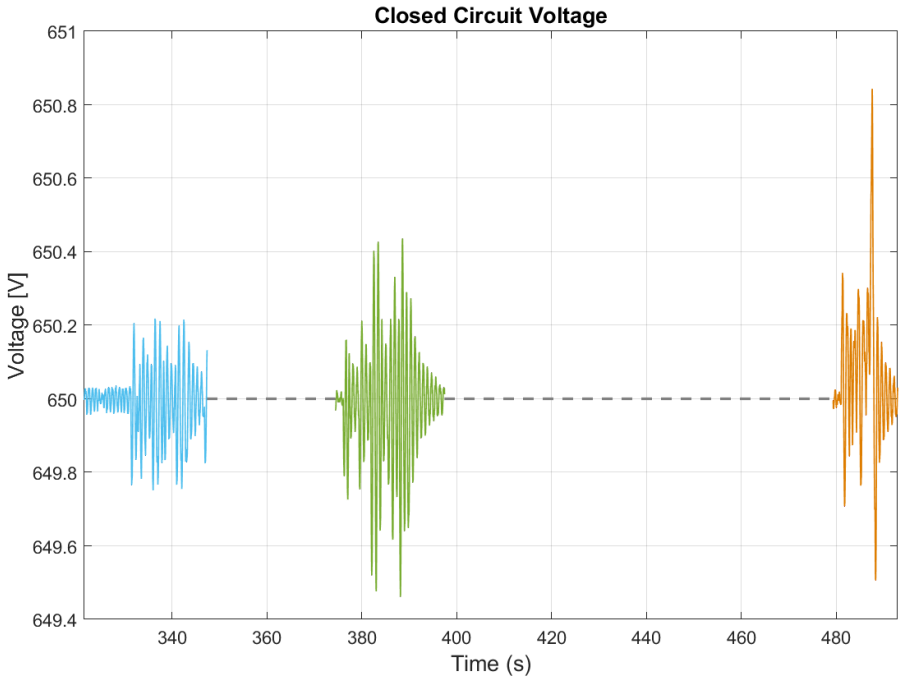

Figure 7.6: Voltage output v_{DC} from the continuous model and v_{out} logged from the physical equipment perfectly correlated.

7.3 Discussion of Laboratory Work

Section 7.2.1 presents the current output i_{out} from the physical sensors and i_k from the simulation model. It is clear that the noise of the physical equipment is significantly larger than the noise in the simulation. When considering the constant current in the first part of the first data log in figure 7.5, the noise from the simulation model is nearly insignificant with a top amplitude of 0.03 A, while the noise of the physical equipment is at top amplitude of 0.72 A. This notable noise from the physical equipment is the result of using sensors rated to higher currents, leading to a sensitive low current operation. It would be interesting to conduct the same tests under similar circumstances with current sensors rated to low current operation, to obtain an improved review of the current output, i_{out}.

In comparing figure 7.5 and figure 7.6, some conclusions can be drawn. The first section leaves the current unchanged for the longest time span: 10 seconds, while the second and third data logs leave the current unchanged for 7 and 5 seconds respectively. In figure 7.6, this shows clearly that within the first ten seconds, the voltage signal is experiencing a noticeably stable behavior. This can also, to a smaller degree, be observed at the end of the second and third data log. The beginning of the second and third data log is initialized at a constant current, which also leads to stable behavior in the voltage outputs.

Section 7.2.2 examines the amplitude of the noise in the voltage output. The first section shows that after t = 331 s, when the current starts to increase, the voltage noise amplitude is also increased. However, the amplitude of the voltage through the current ramp period of the first section is quite similar with no clear peak. This is because the current is increased in a fairly steady process. The largest amplitude of the first section is on 0.249, with a deviation of $38.3 \cdot 10^{-3}\%$ of the mean voltage output at 650 V. The second data log has two clearly larger sections of noise where the current has not been increased as continuously. The voltage deviates most at t = 388 s, at the end of the increasing ramp. The most significant deviation of 649.462 V leads to an $8.28 \cdot 10^{-3}\%$ disparity of the mean voltage output.

The third section is noteworthy. It is the smallest data logging of only 14 seconds. The current is decreasing at a very high rate of 0.36 amperes per second, compared to the rate of 0.1 and 0.13 from the other data logs. As assumed, this leads to a significant voltage deviation. At the time of the steepest decreasing ramp, the voltage level is measured to 650.843 V. This is a 0.13% deviation from the mean voltage output. Despite the deviations and noise even at a constant current, the resulting graphs are within acceptable voltage and current levels. Even in the most discontinuous current rates, the system behaved stable. The voltage signals experienced noise, but always with a mean of 650V, and the signals followed the current signals with a fast response.

The change in current was managed manually by turning a rotary control knob. Consequently, the rate of change of current was not changed at a constant velocity in the data logs. The current change was operated at the slowest rate for the first section, and the highest rate for the third section. The erratic behavior of the current compels for an interesting review of the voltage error, as discussed in this section. However, if the testing were conducted in changing the current with constant rates of amperes per second, it would open to a discussion of how much the current rate affects the voltage noise with more realistic quantitative conclusions.

Chapter 8

Concluding Remarks

This thesis has discussed an energy storage emulation for the application of a low voltage grid connection. The BESS is simulated in the MATLAB/Simulink environment, which illustrated that the battery pack complied with the requirements. A bidirectional DC-DC converter is connected to the energy storage system. The converter behavior is explained, as well as an included part about converter control based on an average model. The voltage and current control were based on PI regulation to ensure system stability. Preceding the laboratory testing, the PHIL technique was implemented to acquire realistic results. In order to obtain the voltage model for the PHIL setup, a discrete model was derived theoretically before it was tested through simulation. This chapter takes on the most essential concluding remarks attained from the process.

An outline of different rechargeable battery types with advantages and disadvantages has been explained. The thesis continued with a lithium-ion battery, mainly due to its high energy density and the lack of memory effect in the battery. The computational battery model was then retrieved from the Simulink/Simscape library. The battery was designed for a load of 15 kW for 5 hours. The design was derived, and the Simulink implementation confirmed that the battery was able to supply the required load. However, the BESS later used with the connection to the converter had a significantly lower current running through the battery. This resulted in a state of charge which is above 99.98% in the entire

simulation time. With employing the stabilized battery current, the discharge curve of the battery showed that the voltage over the battery was within its rated limits.

The bidirectional converter is in the thesis simplified with a boost topology to be applied to step up the voltage from the battery and control the current and voltage of the system. As the objective of the thesis did not include an analysis of the switching frequency ripple, the converter was designed as an average model, due to its advantages with a faster simulation time domain and a less complex design. In the converter control, PI regulators were used both in the outer voltage control and inner current control. For the tuning of the PI voltage regulator, the symmetrical optimum method was applied. The computational results of the converter presented acceptable results. The voltage and current error started with a limited error oscillation, before the errors both stabilized at zero as designed. The converter was modeled to a voltage output of 650 V, which is what was attained from the computational results.

For the laboratory testing, a power hardware in the loop methodology was used. This methodology combines testing of both hardware and software, leading to time and cost-effective testing with realistic results. The PHIL structure included a real-time simulation of the emulated energy storage system connected to a real three-phase VSC device under testing. To send the reference voltage to the controlled voltage source, a discrete model was derived using the trapezoid approximation. From the computational results, it can be concluded with that the discretization algorithm performed in accordance with the goal of mimicking the continuous model, as the signals both in the current and voltage output behaved identically.

To ensure realistic simulation results in view of the experimental validation, noise was added to the computational model in the output voltage and current. The variance of the noise was attained from tests at the Norwegian Smart Grid Laboratory. This lead to a smooth transition from the simulated model to the physical laboratory equipment. The laboratory results from the current signal depicts an acceptable outcome where the current

from the physical signals and the current from the simulated model follows the same values. However, the noise of the physical equipment was significantly larger than the noise in the simulation. This was due to the use of sensors at the laboratory rated to relatively much higher currents, leading to a sensitive low current operation. The voltage signals from the physical laboratory equipment and simulation model responded identically throughout the entire simulation, which describes a successful PHIL test of an emulation of a battery energy storage system.

Further Work

There are numerous ways of taking the system proposed in this thesis further. This section will provide some of the proposals for further work.

The model designed in this thesis included a DC-DC boost converter, with the intention of it to act as a bidirectional converter for the purposes of discharging the battery. It would be interesting to take the model further with the development of an actual bidirectional converter. In that case, the model could also be taken through the charging process of the battery. Different battery types were described in the thesis, but only lithium-ion was used. It would be interesting to see how the other battery types behaved differently and conduct detailed testings of different battery types for an energy storage emulation. The Simulink/Simscape battery from the library can be modeled as different battery types.

The computational model consisting of a DC-DC converter and a battery model can be expanded. This can potentially be modeled as a microgrid. First of all, a voltage source converter can be modeled as in [8] with a voltage and current control and a phase locked loop. This VSC can be connected to an AC grid with a grid forming converter like the one in [8]. The AC grid can be expanded with several VSCs connected to grid sources. A PV model can be implemented from the Simulink/Simscape library with an MPPT to ensure a realistically strong performance. The cloud cover for the PV can be varied either randomly or by implementing actual weather data for a specific geographical area in a MATLAB function implemented in the PV model. This will ensure a PV RES with

relatively realistic behavior. Further, a wind turbine can be implemented to another VSC in the grid. The wind speed can be modeled in the same way as the cloud cover of the PV: either with a random variance or with the implementation of real weather data. Loads should also be implemented in the system to model a microgrid. The decision of what the load should represent depends on the scope of the work. Among others, the loads could copy the behavior of a neighborhood, office buildings, or stores. The load rating should be set as realistic values for the said loads, and with the peak and low load periods at the parts of the day where the grid would usually experience peaks and low load conditions. For instance, a household usually has a high load in the mornings and the evening, and in Norway, the difference between winter and summer should also be taken into consideration. This would lead to a demand for a further advanced control system. A droop based control strategy which has been explained in [8] could further be implemented with power control in the voltage source converters for an improved regulation of the system. The microgrid could alternatively be controlled with a virtual synchronous machine (VSM) scheme. If both control schemes, both droop- and VSM-based, are tested, the microgrid would create a consistent basis of comparison between the control models. With the loads, the PV, the wind turbine(s) and the ESS, as well as a grid forming converter, the model is versatile, and several tweaks can be done to the model to test it for different scenarios.

Oil and gas companies have an increased interest in offshore microgrids, with an implementation of energy storage systems and offshore wind parks to supply oil platforms. This can be further analyzed and tested in Simulink. When the simulation model is developed according to the previous paragraph, the work required to change it to an offshore microgrid would include a higher voltage level of the grid, a higher rating of the wind turbines and a completely different load behavior. A gathering of data from offshore oil platforms would be necessary to model the gas turbines as loads with the ratings realistically obtained.

Bibliography

[1] M. Roser and E. Ortiz-Ospina, *World Population Growth*, 2018. [Online]. Available: https://ourworldindata.org/world-population-growth

[2] I. E. Agency, *World Energy Statistics 2017*, 2017. [Online]. Available: https://www.oecd-ilibrary.org/content/publication/world_energy_stats-2017-en

[3] S. Chakraborty, M. G. Simões, and W. E. Kramer, *Power Electronics for Renewable and Distributed Energy Systems*. Springer, London, 2013.

[4] G. Pepermans, J. Driesen, D. Haeseldonckx, R. Belmans, and W. D'haeseleer, "Distributed generation: definition, benefits and issues," *Energy Policy*, vol. 33, no. 6, pp. 787 – 798, 2005. [Online]. Available: http://www.sciencedirect.com/science/article/pii/S0301421503003069

[5] F. Blaabjerg, Z. Chen, and S. Kjær, "Power electronics as efficient interface of renewable energy sources," vol. 3, 09 2004, pp. 1731 – 1739 Vol.3.

[6] A. Kumar, A. H. Bhat, and P. Agarwal, "Comparative analysis of dual active bridge isolated dc to dc converter with flyback converters for bidirectional energy transfer," in *2017 Recent Developments in Control, Automation Power Engineering (RDCAPE)*, Oct 2017, pp. 382–387.

[7] H. Bai and C. Mi, "Eliminate reactive power and increase system efficiency of isolated bidirectional dual-active-bridge dc–dc converters using novel dual-phase-shift control," *IEEE Transactions on Power Electronics*, vol. 23, no. 6, pp. 2905–2914, Nov 2008.

[8] N. P. Sagatun, “Control structure for islanded microgrids,” Dec 2018.

[9] T. Ackermann, G. Andersson, and L. Södera, “Distributed generation: a definition,” *Electric Power Systems Research*, vol. 57, no. 3, pp. 195–204, 2001.

[10] F. H. Guan, D. M. Zhao, X. Zhang, B. T. Shan, and Z. Liu, “Research on distributed generation technologies and its impacts on power system,” *2009 International Conference on Sustainable Power Generation and Supply*, pp. 1–6, 2009.

[11] Nwulu, N. I., and X. Xia, “Optimal dispatch for a microgrid incorporating renewables and demand response,” *Renewable Energy*, vol. 101, pp. 16–28, 2017.

[12] E. Pritchard, L. Mackey, D. Zhu, D. Gregory, and G. Norris, “Modular electric generator rapid deployment dc microgrid,” *2017 IEEE Second International Conference on DC Microgrids*, pp. 106–110, 2017.

[13] S. Ahmadi, H. Bevrani, S. Shokoohi, and E. Hasanii, “An improved droop control for simultaneous voltage and frequency regulation in an ac microgrid using fuzzy logic,” *Iranian Conference on Electrical Engineering*, vol. 13, no. 23, pp. 1486–1491, 2015.

[14] M. Arlt, G. F. Cardoso, and D. Weng, “Hydrogen storage applications in industrial microgrids,” *2017 IEEE Green Energy and Smart Systems Conference*, pp. 1–6, 2017.

[15] O. M. Toledo, D. O. Filho, and A. S. A. C. Diniz, “Distributed photovoltaic generation and energy storage systems: A review,” *Renewable and Sustainable Energy Reviews*, vol. 14, no. 1, pp. 506 – 511, 2010. [Online]. Available: http://www.sciencedirect.com/science/article/pii/S136403210900207X

[16] C. K. Das, O. Bass, G. Kothapalli, T. S. Mahmoud, and D. Habibi, “Overview of energy storage systems in distribution networks: Placement, sizing, operation, and power quality,” *Renewable and Sustainable Energy Reviews*, vol. 91, pp. 1205 – 1230, 2018. [Online]. Available: http://www.sciencedirect.com/science/article/pii/S1364032118301606

[17] Z. Lu, G. Bao, H. Xu, X. Dong, Z. Yuan, and C. Lu, “Battery energy storage system based power quality management of distribution network,” in *Informatics in Control, Automation and Robotics*, D. Yang, Ed. Berlin, Heidelberg: Springer Berlin Heidelberg, 2012, pp. 599–606.

[18] S. Koohi-Kamali, V. Tyagi, N. Rahim, N. Panwar, and H. Mokhlis, “Emergence of energy storage technologies as the solution for reliable operation of smart power systems: A review,” *Renewable and Sustainable Energy Reviews*, vol. 25, pp. 135 – 165, 2013. [Online]. Available: http://www.sciencedirect.com/science/article/pii/S1364032113002153

[19] P. F. Ribeiro, B. K. Johnson, M. L. Crow, A. Arsoy, and Y. Liu, “Energy storage systems for advanced power applications,” *Proceedings of the IEEE*, vol. 89, no. 12, pp. 1744–1756, Dec 2001.

[20] O. Babacan, W. Torre, and J. Kleissl, “Siting and sizing of distributed energy storage to mitigate voltage impact by solar pv in distribution systems,” *Solar Energy*, vol. 146, pp. 199–208, 04 2017.

[21] K. H. Chua, Y. S. Lim, P. Taylor, S. Morris, and J. Wong, “Energy storage system for mitigating voltage unbalance on low-voltage networks with photovoltaic systems,” *IEEE Transactions on Power Delivery*, vol. 27, no. 4, pp. 1783–1790, Oct 2012.

[22] P. Mercier, R. Cherkaoui, and A. Oudalov, “Optimizing a battery energy storage system for frequency control application in an isolated power system,” *IEEE Transactions on Power Systems*, vol. 24, no. 3, pp. 1469–1477, Aug 2009.

[23] J. Leadbetter and L. Swan, “Battery storage system for residential electricity peak demand shaving,” *Energy and Buildings*, vol. 55, pp. 685 – 692, 2012, cool Roofs, Cool Pavements, Cool Cities, and Cool World. [Online]. Available: http://www.sciencedirect.com/science/article/pii/S0378778812004896

[24] S. Teleke, M. E. Baran, S. Bhattacharya, and A. Q. Huang, “Rule-based control of battery energy storage for dispatching intermittent renewable sources,” *IEEE Transactions on Sustainable Energy*, vol. 1, no. 3, pp. 117–124, Oct 2010.

[25] S. X. Chen, H. B. Gooi, and M. Q. Wang, “Sizing of energy storage for microgrids,” *IEEE Transactions on Smart Grid*, vol. 3, no. 1, pp. 142–151, March 2012.

[26] D. Ravi, B. Reddy, S. S. L., and P. Samuel, “Bidirectional dc to dc converters: An overview of various topologies, switching schemes and control techniques,” *International Journal of Engineering and Technology*, vol. 7, pp. 360–365, 09 2018.

[27] F. Caricchi, F. Crescimbini, F. G. Capponi, and L. Solero, “Study of bi-directional buck-boost converter topologies for application in electrical vehicle motor drives,” in *APEC ’98 Thirteenth Annual Applied Power Electronics Conference and Exposition*, vol. 1, Feb 1998, pp. 287–293 vol.1.

[28] S. Agrawal and R. S. Geetha, “Controllers for voltage source converters,” in *2013 International Conference on Emerging Trends in Communication, Control, Signal Processing and Computing Applications (C2SPCA)*, 2013, pp. 1–8.

[29] V. Chitra, *Fuzzy-Based Matrix Converter Drive for Induction Motor*, 01 2017.

[30] A. Manoloiu, H. A. Pereira, R. Teodorescu, M. Bongiorno, M. Eremia, and S. R. Silva, “Comparison of pi and pr current controllers applied on two-level vsc-hvdc transmission system,” in *2015 IEEE Eindhoven PowerTech*, 2015, pp. 1–5.

[31] F. Blaabjerg, Y. Yang, and K. Ma, “Power electronics - key technology for renewable energy systems - status and future,” *2013 3rd International Conference on Electric Power and Energy Conversion Systems*, pp. 1–6, 2013.

[32] K. M. Son, K. Lee, D. Lee, T. C. E. Nho, and H. Kim, “Grid interfacing storage system for implementing microgrid,” *Transmission Distribution Conference Exposition: Asia and Pacific*, vol. 53, pp. 1–4, 2009.

[33] Proposal/ Contract no.: PL019864, “More microgrids: Advanced architectures and control concepts for more microgrids,” *FP6 STREP*, 2006-2009.

[34] ENK5-CT-2002-00610, “Microgrids: Large scale integration of micro-generation to low voltage grids,” 2003-2005.

[35] K. Sarwagya and P. K. Nayak, “An extensive review on the state-of-art on microgrid protection,” in *2015 IEEE Power, Communication and Information Technology Conference (PCITC)*, Oct 2015, pp. 862–866.

[36] A. Vukojevic, “Lessons learned from microgrid implementation at electric utility,” *2018 IEEE Power Energy Society Innovative Smart Grid Technologies Conference*, pp. 1–5, 2018.

[37] N. Hatziargyriou, “Microgrids architectures and control,” *John Wiley and Sons Ltd*, p. 4, 2014.

[38] Y. Zhou and C. N.-M. Ho, “A review on microgrid architectures and control methods,” in *2016 IEEE 8th International Power Electronics and Motion Control Conference (IPEMC-ECCE Asia)*, May 2016, pp. 3149–3156.

[39] B. Yu, J. Guo, C. Zhou, Z. Gan, J. Yu, and F. Lu, “A review on microgrid technology with distributed energy,” in *2017 International Conference on Smart Grid and Electrical Automation (ICSGEA)*, May 2017, pp. 143–146.

[40] A. Hirsch, Y. Parag, and J. Guerrero, “Microgrids: A review of technologies, key drivers, and outstanding issues,” *Renewable and Sustainable Energy Reviews*, vol. 90, pp. 402 – 411, 2018. [Online]. Available: http://www.sciencedirect.com/science/article/pii/S136403211830128X

[41] C. Wang, J. Yan, C. Marnay, N. Djilali, E. Dahlquist, J. Wu, and H. Jia, “Distributed energy and microgrids (dem),” *Applied Energy*, vol. 210, pp. 685 – 689, 2018. [Online]. Available: http://www.sciencedirect.com/science/article/pii/S0306261917316550

[42] S. Parhizi, H. Lotfi, A. Khodaei, and S. Bahramirad, “State of the art in research on microgrids: A review,” *IEEE Access*, vol. 3, pp. 890–925, 2015.

[43] T. Del Carpio Huayllas, D. Ramos, and R. Vasquez-Arnez, “Microgrid systems: Current status and challenges,” 12 2010, pp. 7 – 12.

[44] Y. Wu, N. Chen, D. Jiang, L. Zhang, L. Qu, and M. Qian, “Study on energy storage system participating in frequency regulation of wind farm based on polyline fuzzy neural network,” in *2018 5th IEEE International Conference on Cloud Computing and Intelligence Systems (CCIS)*, Nov 2018, pp. 1086–1090.

[45] Hongyan Piao, Shifeng Chen, Haichao Lv, and Haoming Liu, “Control strategy of battery energy storage system to participate in the second frequency regulation,” in *2015 International Symposium on Smart Electric Distribution Systems and Technologies (EDST)*, Sep. 2015, pp. 53–57.

[46] P. Stenzel, T. Kannengießer, L. Kotzur, P. Markewitz, M. Robinius, and D. Stolten, “Emergency power supply from photovoltaic battery systems in private households in case of a blackout – a scenario analysis,” *Energy Procedia*, vol. 155, pp. 165 – 178, 2018, 12th International Renewable Energy Storage Conference, IRES 2018, 13-15 March 2018, Düsseldorf, Germany. [Online]. Available: http://www.sciencedirect.com/science/article/pii/S1876610218310129

[47] Y. Liu, C. Lin, and S. Chen, “Analysis of load electricity consumption on a low-voltage distribution system with community energy storages,” in *2017 IEEE 3rd International Future Energy Electronics Conference and ECCE Asia (IFEEC 2017 - ECCE Asia)*, June 2017, pp. 2048–2052.

[48] F. Díaz-González, A. Sumper, O. Gomis-Bellmunt, and R. Villafáfila-Robles, “A review of energy storage technologies for wind power applications,” *Renewable and Sustainable Energy Reviews*, vol. 16, no. 4, pp. 2154 – 2171, 2012. [Online]. Available: http://www.sciencedirect.com/science/article/pii/S1364032112000305

[49] O. Tremblay, L. Dessaint, and A. Dekkiche, “A generic battery model for the dynamic simulation of hybrid electric vehicles,” in *2007 IEEE Vehicle Power and Propulsion Conference*, Sep. 2007, pp. 284–289.

[50] O. Vigerstol, “Nickel cadmium batteries for outside telecom plants,” in *Fourteenth Annual Battery Conference on Applications and Advances. Proceedings of the Conference (Cat. No.99TH8371)*, Jan 1999, pp. 313–317.

[51] M. M. Moorthi, “Field experience with large nickel metal hydride (nimh) batteries in stationary applications,” in *INTELEC 06 - Twenty-Eighth International Telecommunications Energy Conference*, Sep. 2006, pp. 1–7.

[52] D. Gies, “New approaches to safe ventilation of equipment containing lead acid and nicd batteries,” in *2015 IEEE Symposium on Product Compliance Engineering (ISPCE)*, May 2015, pp. 1–5.

[53] M. Gonzalez, F. J. Ferrero, J. C. Anton, and M. A. Perez, “Considerations to improve the practical design of universal and full-effective nicd/nimh battery fast-chargers,” in *APEC ’99. Fourteenth Annual Applied Power Electronics Conference and Exposition. 1999 Conference Proceedings (Cat. No.99CH36285)*, vol. 1, March 1999, pp. 167–173 vol.1.

[54] S. M. Mousavi, S. H. Fathi, and G. H. Riahy, “Energy management of wind/pv and battery hybrid system with consideration of memory effect in battery,” in *2009 International Conference on Clean Electrical Power*, June 2009, pp. 630–633.

[55] S. F. Pensabene and J. W. Gould, “Batteries: Unwanted memory spooks nickel-cadmium cells: New understanding of an undesirable phenomenon is the first step in avoiding it,” *IEEE Spectrum*, vol. 13, no. 9, pp. 33–37, Sep. 1976.

[56] S. Podder and M. Z. R. Khan, “Comparison of lead acid and li-ion battery in solar home system of bangladesh,” in *2016 5th International Conference on Informatics, Electronics and Vision (ICIEV)*, May 2016, pp. 434–438.

[57] “Lithium-ion battery overview,” in *Lighting Global*. International Finance Group., 2012.

[58] C. Orendorff, D. H. Doughty, and E. P. Roth, “General discussion of li ion battery safety.” *Proposed for publication in The ECS Interface.*

[59] T. Guena and P. Leblanc, “How depth of discharge affects the cycle life of lithium-metal-polymer batteries,” in *INTELEC 06 - Twenty-Eighth International Telecommunications Energy Conference*, Sep. 2006, pp. 1–8.

[60] J. McDowall, “Understaning lithium - ion technology.” Saft America Inc., 2008.

[61] X. Liu, P. Wang, and P. C. Loh, “A hybrid ac/dc microgrid and its coordination control,” *IEEE Transactions on Smart Grid*, vol. 2, no. 2, pp. 278–286, June 2011.

[62] S. Sanchez, M. Molinas, M. Degano, and P. Zanchetta, “Stability evaluation of a dc micro-grid and future interconnection to an ac system,” *Renewable Energy*, vol. 62, pp. 649 – 656, 2014. [Online]. Available: http://www.sciencedirect.com/science/article/pii/S096014811300428X

[63] “MATLAB Simscape Power Systems Documentation Battery Toolbox,” R2018a, the MathWorks, Natick, MA, USA.

[64] *Lithium-Ion Battery Datasheet*, EEMB Co., Ltd, 8 2016.

[65] L. Valøen and M. I Shoesmith, “The effect of phev and hev duty cycles on battery and battery pack performance,” 03 2019.

[66] R. Sadoun, N. Rizoug, P. Bartholumeus, B. Barbedette, and P. LeMoigne, “Sizing of hybrid supply (battery-supercapacitor) for electric vehicle taking into account the weight of the additional buck-boost chopper,” in *2012 First International Conference on Renewable Energies and Vehicular Technology*, March 2012, pp. 8–14.

[67] H. C. Hesse, M. Schimpe, D. Kucevic, and A. Jossen, “Lithium-ion battery storage for the grid—a review of stationary battery storage system design tailored for applications in modern power grids,” *Energies*, vol. 10, no. 12, 2017. [Online]. Available: http://www.mdpi.com/1996-1073/10/12/2107

[68] *Lithium-Ion Battery Specification*, EEMB Co., Ltd, 2 2016.

[69] N. Mohan, T. M. Undeland, and W. P. Robbins, *Power Electronics. Converters, Applications and Design*, 3rd ed. John Wiley and Sons, Inc, 2003.

[70] M. Matar and R. Iravani, “Fpga implementation of the power electronic converter model for real-time simulation of electromagnetic transients,” *IEEE Transactions on Power Delivery*, vol. 25, no. 2, pp. 852–860, April 2010.

[71] J. Channegowda, B. Saritha, H. R. Chola, and G. Narayanan, "Comparative evaluation of switching and average models of a dc-dc boost converter for real-time simulation," in *2014 IEEE International Conference on Electronics, Computing and Communication Technologies (CONECCT)*, Jan 2014, pp. 1–6.

[72] A. Harumwidiah, M. Ashari, and D. C. Riawan, "Modelling back-to-back converter with average model in wind power system using dfig," in *IPTEK, Journal of Proceeding Series*, vol. 1, 2014, pp. 435–440.

[73] C. Jaen, R. Pindado, J. Pou, and V. Sala, "Adaptive model applied to pwm dc-dc converters using averaging techniques," in *2006 IEEE International Symposium on Industrial Electronics*, vol. 2, July 2006, pp. 1347–1352.

[74] A. Davoudi, J. Jatskevich, P. L. Chapman, and A. Khaligh, "Averaged-switch modeling of fourth-order pwm dc–dc converters considering conduction losses in discontinuous mode," *IEEE Transactions on Power Electronics*, vol. 22, no. 6, pp. 2410–2415, Nov 2007.

[75] F. R. Quintela, R. C. Redondo, N. R. Melchor, and M. Redondo, "A general approach to kirchhoff's laws," *IEEE Transactions on Education*, vol. 52, no. 2, pp. 273–278, May 2009.

[76] S. Sanchez, "Stability investigation of power electronics systems - a microgrid case," *Thesis for the degree of Philosopiae Doctor*, 2015.

[77] S. Sanchez, G. Bergna, and E. Tedeschi, "Tuning of control loops for grid-connected modular multilevel converters under a simplified port representation for large system studies," in *2017 Twelfth International Conference on Ecological Vehicles and Renewable Energies (EVER)*, April 2017, pp. 1–8.

[78] S. Sanchez, S. D'Arco, A. Holdyk, and E. Tedeschi, "An approach for small scale power hardware in the loop emulation of hvdc cables," in *2018 Thirteenth International Conference on Ecological Vehicles and Renewable Energies (EVER).*

[79] OPAL - RT, "POWER HIL (P-HIL): A Revolution in the Industry," Web Site Presentation. [Online]. Available: https://www.opal-rt.com/power-hardware-in-the-loop/

[80] M. Lauritzsen, “Hardware-in-the-loop testing systems for rov control systems,” 2014. [Online]. Available: http://hdl.handle.net/11250/238916

[81] D. Maclay, “Simulation gets into the loop,” *IEE Review*, vol. 43, no. 3, pp. 109–112, May 1997.

[82] W. Adiprawita, A. Suwandi Ahmad, and J. Sembiring, “Hardware in the loop simulation for simple low cost autonomous uav (unmanned aerial vehicle) autopilot system research and development,” 01 2007.

[83] E. R. Mueller, “Hardware -in -the -loop simulation design for evaluation of unmanned aerial vehicle control systems,” 08 2007.

[84] D. Jung and P. Tsiotras, “Modeling and hardware-in-the-loop simulation for a small unmanned aerial vehicle,” vol. 1, 05 2007.

[85] N. Schetinin, N. Moriz, B. Kumar, A. Maier, S. Faltinski, and O. Niggemann, “Why do verification approaches in automation rarely use hil-test?” in *2013 IEEE International Conference on Industrial Technology (ICIT)*, Feb 2013, pp. 1428–1433.

[86] J. Langston, K. Schoder, M. Steurer, O. Faruque, J. Hauer, F. Bogdan, R. Bravo, B. Mather, and F. Katiraei, “Power hardware-in-the-loop testing of a 500 kw photovoltaic array inverter,” in *IECON 2012 - 38th Annual Conference on IEEE Industrial Electronics Society*, Oct 2012, pp. 4797–4802.

[87] R. S. Kaarthik, J. Maisonneuve, and P. Pillay, “Real-time emulation of a pressure-retarded osmotic power generation system,” *IEEE Transactions on Industry Applications*, vol. 53, no. 6, pp. 5768–5776, Nov 2017.

[88] Seung-Ho Song, Byoung-Chang Jeong, Hye-In Lee, Jeong-Jae Kim, Jeong-Hun Oh, and G. Venkataramanan, “Emulation of output characteristics of rotor blades using a hardware-in-loop wind turbine simulator,” in *Twentieth Annual IEEE Applied Power Electronics Conference and Exposition, 2005. APEC 2005.*, vol. 3, March 2005, pp. 1791–1796 Vol. 3.

[89] S. Lentijo, S. D'Arco, and A. Monti, "Comparing the dynamic performances of power hardware-in-the-loop interfaces," *IEEE Transactions on Industrial Electronics*, vol. 57, no. 4, pp. 1195–1207, April 2010.

[90] A. Schmitt, J. Richter, U. Jurkewitz, and M. Braun, "Fpga-based real-time simulation of nonlinear permanent magnet synchronous machines for power hardware-in-the-loop emulation systems," in *IECON 2014 - 40th Annual Conference of the IEEE Industrial Electronics Society*, Oct 2014, pp. 3763–3769.

[91] A. Schmitt, M. Gommeringer, J. Kolb, and M. Braun, "A high current, high frequency modular multiphase multilevel converter for power hardware-in-the-loop emulation," in *PCIM Europe 2014; International Exhibition and Conference for Power Electronics, Intelligent Motion, Renewable Energy and Energy Management*, May 2014, pp. 1–8.

[92] M. Karpenko and N. Sepehri, "Hardware-in-the-loop simulator for research on fault tolerant control of electrohydraulic flight control systems," in *2006 American Control Conference*, June 2006, pp. 7 pp.–.

[93] A. Allegre, A. Bouscayrol, J. Verhille, P. Delarue, E. Chattot, and S. El-Fassi, "Reduced-scale-power hardware-in-the-loop simulation of an innovative subway," *IEEE Transactions on Industrial Electronics*, vol. 57, no. 4, pp. 1175–1185, April 2010.

[94] C. Mayet, A. Bouscayrol, P. Delarue, E. Chattot, and I. Dekik, "Reduced-scale-power hardware-in-the-loop simulation of a subway line," in *2015 IEEE Vehicle Power and Propulsion Conference (VPPC)*, Oct 2015, pp. 1–6.

[95] J. Balchen, T. Andresen, and B. Foss, *Reguleringsteknikk*. NTNU, Institutt for teknisk kybernetikk, 2004. [Online]. Available: https://books.google.no/books?id=2L_HtQEACAAJ

[96] A. A. Giordano and A. H. Levesque, *Getting Started with Simulink*. Wiley, 2015. [Online]. Available: https://ieeexplore.ieee.org/document/8044034

[97] *COMPISO System Unit 200-1GAMP6*, EGSTON Power, 2019.

[98] S. S. Noureen, V. Roy, and S. B. Bayne, “An overall study of a real-time simulator and application of rt-lab using matlab simpowersystems,” in *2017 IEEE Green Energy and Smart Systems Conference (IGESSC)*, Nov 2017, pp. 1–5.

Appendices

Appendix A

Academic Paper

The academic paper includes some of the most important findings and results from the thesis. The paper is written as a contribution to the International Conference on Environment and Electrical Engineering (EEEIC) 2019.

Energy Storage Emulation in Islanded Low Voltage Grid

Nora Plassbak Sagatun
Department of Electric Power Engineering
Norwegian University of Science and Technology
Trondheim, Norway
nora.sagatun@gmail.com

Santiago Sanchez
Department of Electric Power Engineering
Norwegian University of Science and Technology
Trondheim, Norway
santiags@ntnu.no

Elisabetta Tedeschi
Department of Electric Power Engineering
Norwegian University of Science and Technology
Trondheim, Norway
elisabetta.tedeschi@ntnu.no

***Abstract*—With an increased integration of grid-connected distributed generators in the power systems, the control structures are increasingly complex. This paper discusses a distributed energy storage technology based on battery banks. The energy storage is connected to a bidirectional DC-DC converter. The design of the battery pack and control of the converter is included in the paper. Additionally, the energy storage system is emulated with a laboratory setup through the use of a power hardware in the loop architecture. The simulations are carried out in MATLAB/Simulink and Opal-RT.**

***Index Terms*—ESS, battery system, bidirectional converter, converter control, PHiL**

I. Introduction

The electrical grid is in the midst of a significant transition. As the world's population continue to grow, more people are in need for electricity as well as the ever attention to climate change mitigation is growing. This has lead to several arising trends regarding the electricity grid. One of the clearest and most impacting of the trends is the growing use of distributed generators. When a distributed generator is connected to the distribution grid, it requires advanced control and regulation to avoid fault in system resonance and interference [1].

The technology behind DGs includes renewable energy sources (RES), non renewable electricity generators and energy storage systems (ESS). Common renewable energy sources used in distributed generation may include photovoltaic systems (PV) and wind energy systems. Distributed energy resources (DER) also include controllable loads such as plug in vehicles and power electronic loads [2], [3]. Due to the intermittent behaviour of RESs, energy storage systems play a crucial role within the power distribution in a low-voltage grid. Battery systems and hydrogen storage systems, as well as flywheels are primarily used as ESS. The implementation of ESSs supports the inertia of the grid, hence decreasing the chance of instability [4]. This is particularly important when the grid has a high degree of stochastic load penetration.

A bidirectional DC-DC converter is widely used in the ESS application, particularly in low voltage grids. The bidirectional converter connects the energy storage technology to an additional converter that links the DC side with the AC grid (see Fig. 1). An application of the energy storage system as seen in Fig. 1 requires an additional two-level voltage source converter to coordinate the power flow between the AC and DC buses. The converter's bidirectional characteristic allows for power flow both ways. This leads to an improved performance of the system as the converter allows for an efficient control of the voltage levels [5], [6].

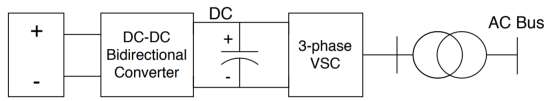

Fig. 1. Line diagram of paper scope

The paper opens with an explanation of the battery model used in the study. Further, a section on the bidirectional converter explains its behaviour and the control using Proportional - Integral (PI) regulators for voltage and current stability. Section 4 explains the Power Hardware in the Loop (PHiL) technique used to carry out laboratory testing and explains the discretization algorithm used to achieve the provided results. The computational results from implementation of the battery bank and discretized converter is given in section 5, along with the final laboratory testing results.

II. Battery System

A. Battery Model

The state of charge (SOC) of the battery can be expressed as in equation (1) [7], [8].

$$SOC = 100(1 - \frac{\int i_b dt}{Q}) \tag{1}$$

Where i_b is the battery current and Q is the battery capacity. The terminal voltage V_b is calculated as shown in (2). The open circuit voltage is expressed as V_0, the internal resistance is denoted R_b. K denotes the polarization voltage. A and B are the exponential zone voltage and the exponential capacity respectively.

$$E_{batt} = E_0 + R_b \cdot i_b - K\frac{Q}{Q + \int i_b dt} + A \cdot exp(-B \int i_b dt) \tag{2}$$

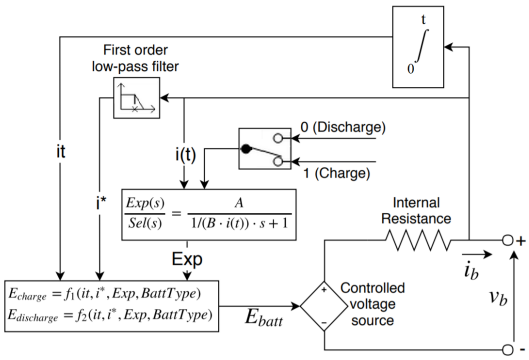

Fig. 2. Equivalent battery model from Simulink.

In the conceptual scheme in Fig. 2, E_{batt} is the nonlinear voltage. $Exp(s)$ denotes the exponential zone dynamics and $Sel(s)$ represents the battery mode, where $Sel(s) = 0$ when the battery is discharging and 1 when the battery is charging. $i*$, i_b and it are respectively the low frequency current dynamics, the battery current and the extracted capacity.
The discharge model of the Lithium-Ion battery is given in (3) and the charge model is given in (4).

$$f_1(it, i*, i) = E_0 - K \cdot \frac{Q}{Q - it} \cdot i* - K \cdot \frac{Q}{Q - it} \cdot it + A \cdot exp(-B \cdot it) \quad (3)$$

$$f_2(it, i*, i) = E_0 - K \cdot \frac{Q}{it + 0.1 \cdot Q} \cdot i* - K \cdot \frac{Q}{Q - it} \cdot it + A \cdot exp(-B \cdot it) \quad (4)$$

B. Internal resistance

The battery's internal resistance has a significant impact on the voltage drop caused by current deviation. Reference [9] discovered a mismatch between the internal resistance provided by the manufacturer's data sheet and the current variation. Therefore, a new relation was proposed as in equation (5).

$$\eta = 1 - \frac{I_{nom} \cdot R}{V_{nom}} \quad (5)$$

Where η is the efficiency coefficient. The nominal discharge curve is dependent on the rated current, I_{nom}, which therefore can be expressed as in (6).

$$I_{nom} = Q_{nom} \cdot 0.2/1hr \quad (6)$$

Substituting (5) and (6) allows the expression of the internal battery resistance as a function of the nominal voltage, the efficiency and the nominal capacity.

$$R = V_{nom} \cdot \frac{1 - \eta}{0.2 \cdot Q_{nom}} \quad (7)$$

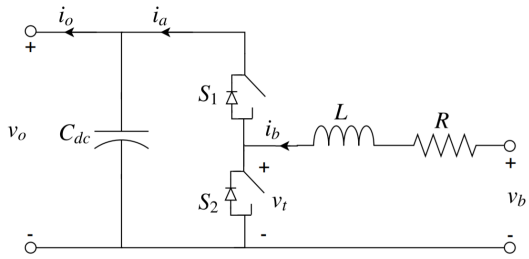

(a) Bidirectional Converter Topology.

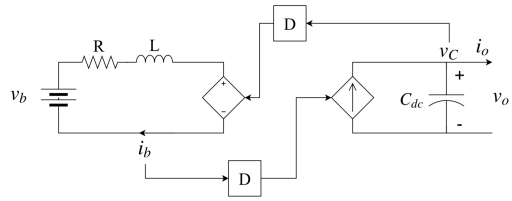

(b) Boost converter average model.

Fig. 3. Bidirectional Converter.

III. Bidirectional Converter

A. Converter Behaviour

Figure 3a shows a boost converter, where the witches are operated in a complementary fashion. Hence, when the first switch, S_1 is on, the second switch, S_2, is off and vice versa. In binary form the open switch is denoted as $S = 0$ and the closed switch, when the switch is on, is denoted as $S = 1$.

B. Converter Control

1) Inner Current Control Loop: PI regulators are used in both the current and voltage control for the bidirectional converter [10]. In the boost converter topology in Fig. 3a, the battery voltage expression is:

$$v_b = Ri_b + \frac{Ldi_b}{dt} + v_t \quad (8)$$

Where v_t equals v_{out} when S_1 is closed. When S_1 is open, v_t will be 0. This gives the expression of v_t as in (9) .

$$v_t = v_o \cdot S_1 \quad (9)$$

In (8), the controlled link is $v_o S_1$, which further is expressed as μ.

$$\frac{Ldi_b}{dt} = v_b - Ri_b - \mu \quad (10)$$

The losses of Ri_b can be neglected when tuning the PI regulator.

$$K_p(i_b^* - i_b) + K_i \int_0^t (i_b^* - i_b)dt = v_b - \mu \quad (11)$$

Here, i_b^* is the reference current of the battery. The difference from the reference current to the actual current is the system error and is denoted e.

$$\mu = -(K_p e + K_i \int_0^t edt) + v_b \quad (12)$$

Expanding μ gives a further expression of the average duty value (D). To simplify the expression, the the output voltage can be approximated at its nominal value $\overline{v_o}$:

$$D = [-(K_p e + K_i \int_0^t edt) + v_b] \cdot \frac{1}{\overline{v_o}} \tag{13}$$

The analog sensors of the current controller is denoted as T_a and the time constant of the controller is expressed as in (14)

$$\tau = \frac{L}{\omega_b R} \tag{14}$$

Where ω_b is the base angular frequency, and L and R are the inductance and resistance, respectively. From this, the current proportional gain K_p and the current integral gain, K_i can be calculated.

$$K_p = \frac{L}{2\omega_b T_a}, \quad K_i = \frac{K_p}{\tau} \tag{15}$$

2) Outer Voltage Control Loop: Following the alternating current i_a in figure 3a, it can be observed that the current equals i_b when S_1 is on, and that the current is 0 when S_2 is off. Consequently, i_a can be expressed as:

$$i_a = i_b \cdot S_1 \tag{16}$$

The current dynamics can be written as in (17).

$$i_a - i_o = C_{dc} \frac{dv_o}{dt} \tag{17}$$

The controllable signal i_a is denoted as μ_v. Denoting the deviation between the reference voltage and v_o as the error e_v, the expression of μ_v becomes:

$$\mu_v = K_{pv} \cdot e_v + K_{iv} \int_0^t edt + i_o \tag{18}$$

In the voltage control loop design, it is possible to use an approximation model of the current controlled loop. This approximation uses a first order model with a time constant T_e. The time constant T_e is calculated as in (19) [10].

$$T_e = 2 \cdot T_a \tag{19}$$

Where, T_a is the time constant used in the current controller for i_b described above. The proportional characteristics between i_a and i_b allows the hierarchical control strategy. The dynamic of system modelled is given in (20).

$$C_{dc} \frac{dv_o}{dt} = i_a - i_o \tag{20}$$

Where i_a is the proportional current of the inner loop as seen in figure 3a. The PI voltage controller has been tuned by applying symmetrical optimum to the per unit system inn accordance of Ref. [10].

$$K_{pv} = \frac{\omega_m \cdot C_{pu}}{\omega_b}, \quad K_{iv} = z \cdot K_{pv} \tag{21}$$

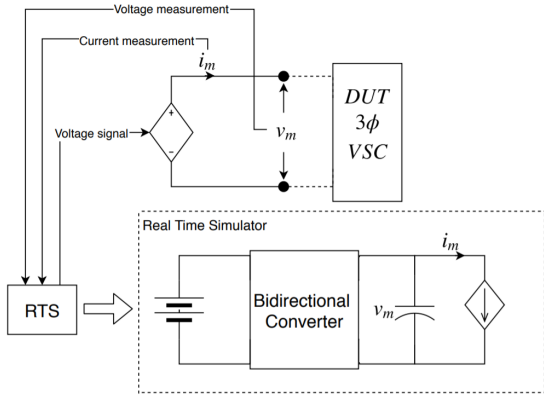

Fig. 4. Outline of PHiL Structure for emulation of ESS.

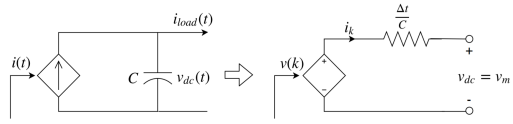

Fig. 5. Illustration of discretization objective.

IV. Power Hardware in the Loop

A. PHiL Structure

Results based on simulations have the risk of differing between different programs, mathematical models and complexity of the model. On the other hand, laboratory experiments usually comes at a high cost and requires a long developing period. Therefore, the PHiL technique is in this case used to test the system dynamics and acquire realistic results [3], [11]. The system outline is defined in Fig. 4. The converter circuit is based on an average model of the boost converter and connected to the Device Under Testing (DUT) which is a three-phase voltage source converter. From there, the measurements of voltage and current are signaled to the Real Time Simulator (RTS). The RTS simulates the energy storage model connected to the bidirectional converter and a load. As illustrated, a voltage source model is required to send the voltage reference to the controlled voltage source. In order to obtain the voltage model a discrete model at the capacitor of Fig. 4 is obtained in the following subsection

B. Discretization Algorithm

The aim of the discretization is to model the parallel connection of a current controlled source and the capacitor into its Thevenin equivalent circuit, as represented in Fig. 5. This procedure enables an emulation of the energy storage system up to the current controlled source of the high voltage side of the converter.

The Kirchhoff's current law can be described as:

$$C\frac{dv_{dc}(t)}{dt} = i(t) - i_{load}(t) \tag{22}$$

where, i(t) is controllable and $i_{load}(t)$ is the disturbance. The expression can further be represented in the Laplace domain as in (23).

$$CsV_{DC}(s) = I(s) - I_{load}(s) \tag{23}$$

where, $V_{DC}(s), i(s)$ and $i_{load}(s)$ are the same variables as above in the Laplace domain.

The trapezoidal approach of discretizing continuous signals leads to:

$$s = \frac{2(z-1)}{T(z+1)} \tag{24}$$

The system in the z-domain is represented as follows:

$$C\frac{2(z-1)}{T(z+1)}V_{dc}(z) = I(z) - I_{load}(z) \tag{25}$$

$$2C(z-1)V_{dc}(z) = T(z+1)I(z) - T(z+1)I_{load}(z) \tag{26}$$

The trapezoidal approach obtains a signal multiplied with z equals the signal one sample time ahead. This is implemented in discrete form (27) and reordered in (28).

$$v_{dc,k+1} - v_{dc,k} = \frac{T}{2C}(i_{k+1} + i_k) - \frac{T}{2C}(i_{L,k+1} + i_{L,k}) \tag{27}$$

$$v_{dc,k+1} = v_{dc,k} + \frac{T}{2C}(i_{k+1} + i_k - i_{L,k+1} - i_{L,k}) \tag{28}$$

Now using the instant time current gives the following expression in (29). (29) is used in the computational model to obtain the same signals as the continuous time model.

$$v_{dc,k} = v_{dc,k-1} + \frac{T}{2C}(i_k - i_{k-1} - i_{L,k-1} - i_{L,k}) \tag{29}$$

Finally, the circuit at the right had of Fig. 5 can be obtained from (29). Therefore, $\Delta t = \frac{T}{2}$, the voltage drop is obtained with the measured current i_k and the computed resistor $\Delta t/C$, the output voltage is $v_m = v_{dc,k}$ and the controlled voltage source is calculated with the remaining part of the terms.

V. Computational Results

A. Design of Battery

The design of the battery pack is based upon data sheet [12]. The battery system is modelled to supply a load of 15 kW for 5 hours. Consequently, the energy capacity of the ESS is 75 kWh. The output voltage v_b is modelled to 48 V and is intended to be connected to a boost converter.

Nominal voltage of one battery cell is given at 3.7 V. The output voltage is dependent on the number of battery cells connected in series. The number of batteries in series is calculated as the fraction of the total battery voltage and the voltage of one battery cell. This leads to final n_s of 13. The capacity required of battery pack is obtained from the system load and output voltage, which gives a capacity of 1559.25 Ah. The capacity per cell is given as 2.6 Ah. The capacity of the battery pack is dependent on the number of batteries in parallel.

$$n_p = \frac{1559.25}{2.6} = 599.71 \approx 600 \tag{30}$$

The battery efficiency coefficient of a lithium-ion battery is typically $80 - 90\%$ [13]. It is assumed that the battery pack holds an efficiency of 90%. The internal impedance given in the data sheet is set to $\leqslant 180$ mΩ. However, considering section II-B, the internal impedance will be calculated according to (7), resulting in R = 0.0154 Ω.

TABLE I
Battery Block Parameters

Parameter	Value
Nominal Voltage (V)	48.1
Rated Capacity (Ah)	1559.25
Cut-off Voltage (V)	39
Fully Charged Voltage (V)	54.6
Nominal Discharge Current (A)	312
Internal Resistance (Ohms)	0.0154
Capacity at Nominal Voltage (Ah)	1560
Exponential Zone Voltage (V)	51.86
Exponential Zone Capacity (Ah)	76.61

B. Energy Storage Implementation in Simulink

All the retrieved values are collected in table I and implemented in the Simulink battery model. The data regarding voltages were retrieved from the data sheet and multiplied with n_s, while the capacity and current values were multiplied with n_p as described above.

Figure 6 illustrates the nominal discharge characteristic curve of the battery using the model values from Table I. The nominal discharge current is set at $312A$. The exponential voltage drop when the battery is charged is represented by the yellow section of the graph. This section lasts from $t = 0$ to $t = 0.23$ which is at 13.8 minutes. The second zone is the area in where the charge can be extracted from the battery until the voltage is below the nominal voltage. The nominal voltage is here set to the default value of $7.2V$. After this, the voltage drops rapidly and this section represents the total discharge of the battery at 5 hours.

C. Discretization of Converter

To ensure realistic simulation results in view of the experimental validation, noise was added to the computational model in the output voltage and current. The variance of the noise is attained from tests at the Norwegian Smart Grid Laboratory. Voltage variance is set to 0.1150 and current variance is set to 0.0609. The model setup of the energy storage system has a low capacitance from design. Besides, the capacitor in the physical converter at the laboratory has a value of $14mF$ which is larger. Additionally, the current step from 1

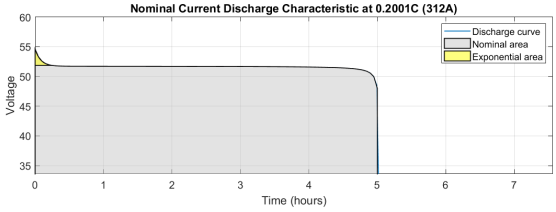

Fig. 6. The nominal discharge curve of the battery.

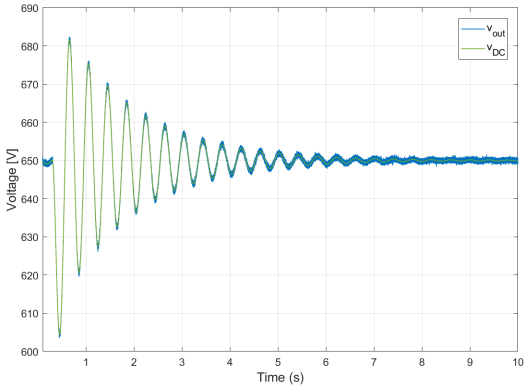

Fig. 7. Voltage output V_{out} from the continuous model and v_{DC} from the discrete model.

to 12 amperes is relatively big. This causes a slow response which leads to large and low frequency oscillation in both the voltages and currents. Figure 7 shows that the voltages of the continuous and discretized model behave similarly, with the initial oscillation before both stabilize at the desired output voltage of $650V$. The currents in Fig. 8 also show corresponding performance with the added noise.

D. Laboratory Implementation

The laboratory testing was conducted in the Norwegian Smart Grid Laboratory (see Fig. 9). The model was implemented with an OPAL - RT simulator with a sampling time $Ts = 100\mu$s, which signalled the physical laboratory equipment. The following results in Fig. 10 and 11 are obtained from a closed loop test at three different sections from logging. The blue section represents an initial steady state operation before the current is gradually increased, which also increases the amplitude of the voltage noise. The green section shows a further increase in current, while the orange section represents the section of fast decrease which gives the largest impact on the voltage. The dashed gray line between the logged signals are the estimated average value of respectively voltages and currents. Figure 10 depicts the voltage graph with an average voltage level of $650V$. Figure 11 shows the current i_k from

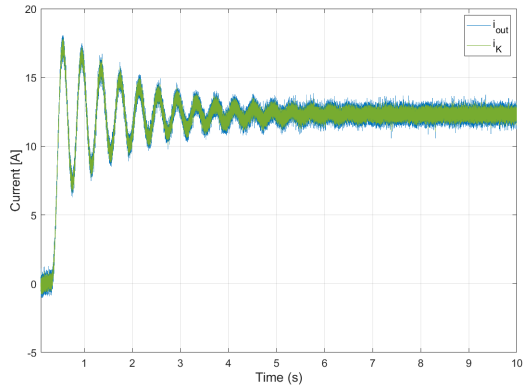

Fig. 8. Current output i_{out} from the continuous model and i_K from the discrete model.

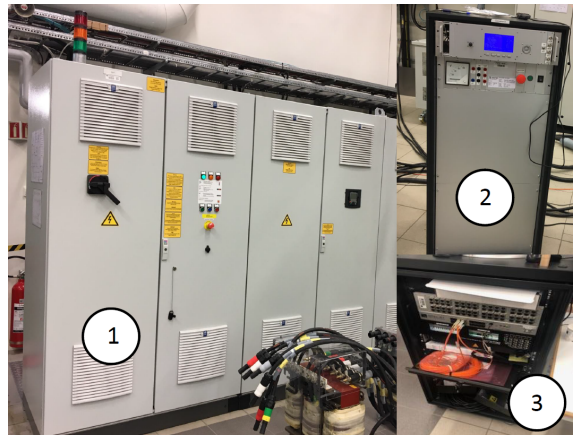

Fig. 9. Norwegian Smart grid Laboratory. (1): 200kVA Controlled Voltage Source, (2): 60 kVA $3-\phi$ VSC, (3): OPAL-RT.

the physical measurement as the black line which is always within the continuous model current i_{out}.

VI. Concluding Remarks

This paper discusses an energy storage emulation for the application of low voltage grid connection. A battery modelled is described theoretically and designed to meet set requirements. The ESS is simulated in the MATLAB/Simulink environment, which illustrated that the battery pack complied with the requirements. A bidirectional DC-DC converter is connected to the energy storage pack. The converter behaviour is explained, as well as an included part about converter control based on an average model. The voltage and current control was based on PI regulation to ensure system stability. Preceding the laboratory testing, the PHiL technique was implemented to acquire realistic results. In order to obtain the voltage model

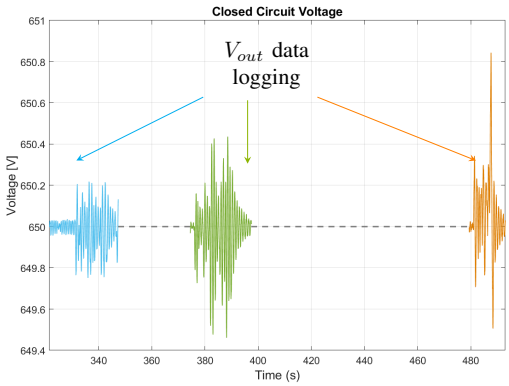

Fig. 10. Voltage output V_{out} from the continuous model and v_{DC} logged from the physical equipment perfectly correlated. Blue: first storing data in ramp test. Green: second storing data in ramp test. Orange: Third storing data current decreasing ramp. The gray dashed line represents a constant estimated average between data loggings.

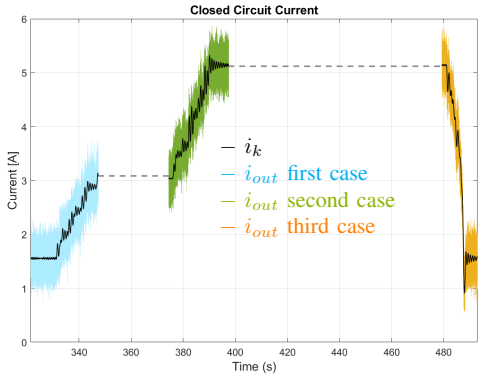

Fig. 11. Current output i_{out} from the continuous model and i_K i_k from the physical measurement as the black line. Blue: first storing data in ramp test. Green: second storing data in ramp test. Orange: Third storing data current decreasing ramp. The gray dashed line represents a constant estimated average between data loggings.

for the PHiL setup, a discrete model was derived theoretically before it was tested through simulation. The computational results presented acceptable outputs. The laboratory implementation was conducted and presented an identical voltage behaviour in the simulated and physical measurements. The current results were also achieved according to the desired output. The notable noise in the current graph is the result of using sensors rated to much higher currents, leading to a sensitive low current operation.

REFERENCES

[1] E. Pritchard, L. Mackey, D. Zhu, D. Gregory, and G. Norris, "Modular electric generator rapid deployment dc microgrid," *2017 IEEE Second International Conference on DC Microgrids*, pp. 106–110, 2017.

[2] Nwulu, N. I., and X. Xia, "Optimal dispatch for a microgrid incorporating renewables and demand response," *Renewable Energy*, vol. 101, pp. 16–28, 2017.

[3] W. Zaixing, F. Fei, L. J. Seng, S. K. Yak, X. Liu, M. A. Zagrodnik, and A. K. Gupta, "Reduction of common mode voltage of 2-level voltage source inverter-fed machine," in *2017 Asian Conference on Energy, Power and Transportation Electrification (ACEPT)*, 2017, pp. 1–5.

[4] F. A. Inthamoussou, J. Pegueroles-Queralt, and F. D. Bianchi, "Control of a supercapacitor energy storage system for microgrid applications," *IEEE Transactions on Energy Conversion*, vol. 28, no. 3, pp. 690–697, 2013.

[5] L. Ni, D. J. Patterson, and J. L. Hudgins, "High power current sensorless bidirectional 16-phase interleaved dc-dc converter for hybrid vehicle application," *IEEE Transactions on Power Electronics*, vol. 27, no. 3, pp. 1141–1151, March 2012.

[6] X. Li, W. Zhang, H. Li, R. Xie, and D. Xu, "Design and control of bi-directional dc/dc converter for 30kw fuel cell power system," in *8th International Conference on Power Electronics - ECCE Asia*, May 2011, pp. 1024–1030.

[7] X. Liu, P. Wang, and P. C. Loh, "A hybrid ac/dc microgrid and its coordination control," *IEEE Transactions on Smart Grid*, vol. 2, no. 2, pp. 278–286, June 2011.

[8] S. Sanchez, M. Molinas, M. Degano, and P. Zanchetta, "Stability evaluation of a dc micro-grid and future interconnection toan ac system," *Renewable Energy*, vol. 62, pp. 649 – 656, 2014. [Online]. Available: http://www.sciencedirect.com/science/article/pii/S096014811300428X

[9] O. Tremblay, L. Dessaint, and A. Dekkiche, "A generic battery model for the dynamic simulation of hybrid electric vehicles," in *2007 IEEE Vehicle Power and Propulsion Conference*, Sep. 2007, pp. 284–289.

[10] S. Sanchez, G. Bergna, and E. Tedeschi, "Tuning of control loops for grid-connected modular multilevel converters under a simplified port representation for large system studies," in *2017 Twelfth International Conference on Ecological Vehicles and Renewable Energies (EVER)*, April 2017, pp. 1–8.

[11] S. Sanchez, S. D'Arco, A. Holdyk, and E. Tedeschi, "An approach for small scale power hardware in the loop emulation of hvdc cables," in *2018 Thirteenth International Conference on Ecological Vehicles and Renewable Energies (EVER)*, April 2018, pp. 1–8.

[12] *Lithium-Ion Battery*, EEMB Co., Ltd, 8 2016.

[13] L. Valen and M. I Shoesmith, "The effect of phev and hev duty cycles on battery and battery pack performance," 03 2019.

Appendix B

Computational Result: Charge of Battery

In the charging of the battery, the battery model is designed as in accordance with section 3.3. However, the DC-DC converter and control system is disconnected, as the system is modelled for the discharging process. The battery is set to start of fully discharged, with a SOC of 0 $\%$, and is charged to the SOC of 0.01238 $\%$ after ten seconds. This leads to an average charge of $1.238 \cdot 10^{-3}\%$ per second. The circuit consists of a battery and a controlled current source set to 69.5 A to obtain a good basis of comparison to the discharge results. This is shown through the results in figure B.1 as a negative current flow i_b through the battery. The voltage is increasing from 109.29 V to 109.37 V.

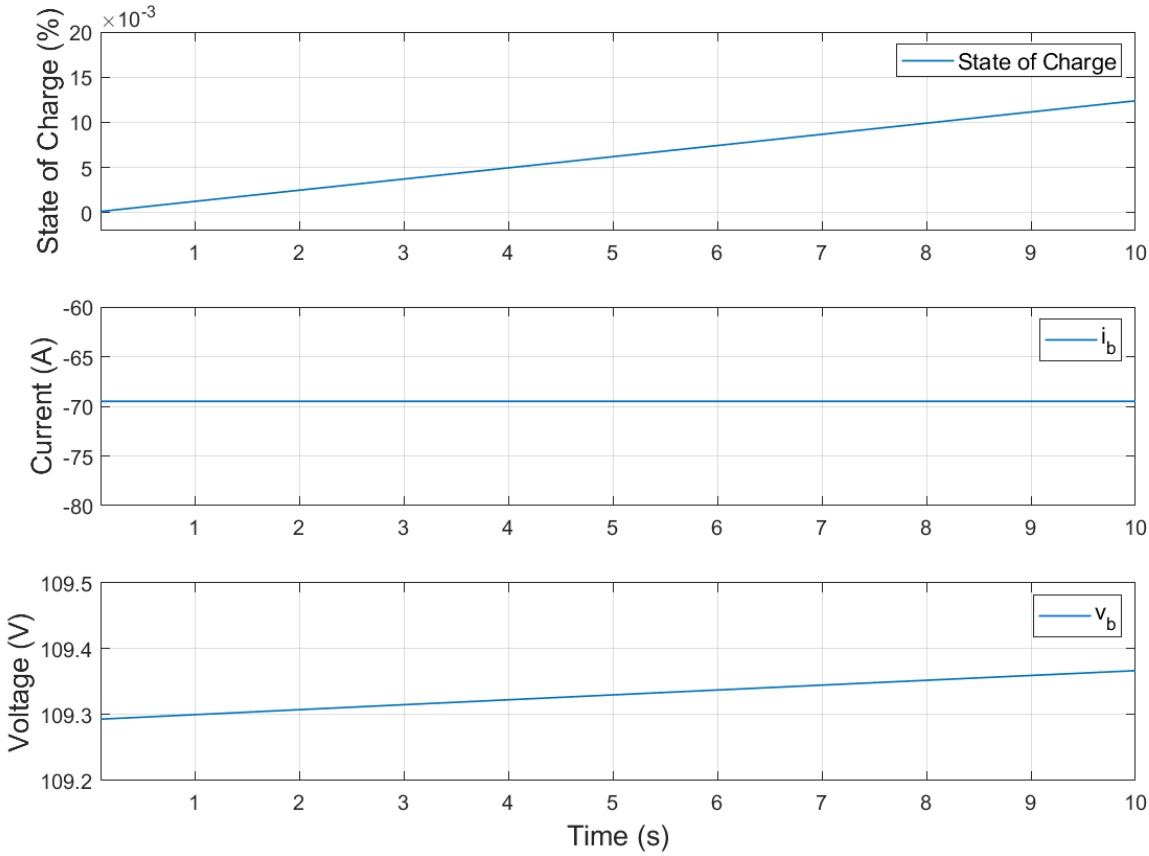

Figure B.1: Resulting graphs from charging the battery model. The top graph shows the state of charge, the middle graph is the current out from the battery and the bottom graph shows the voltage over the battery system.

Appendix C

Computational Models

C.1 Computation Model for sections 6.1 and 6.2

Figures C.1, C.2 and C.3 presents the computational Simulink model which enabled the results presented in sections 6.1 and 6.2. Figure C.1 depicts the setup for the boost converter average model with the battery. Figure C.2 shows the current and voltage control of the system, where the voltage control has the green background and the current controllers has the blue background. Figure C.3 shows the system setup and the powergui. For the use of a real time simulator, it is required that all circuits are placed in one sub-module, while the scopes are placed in another sub-module. Figures C.2 and C.3 are left unchanged when obtaining the results in the other sections of chapter 6.

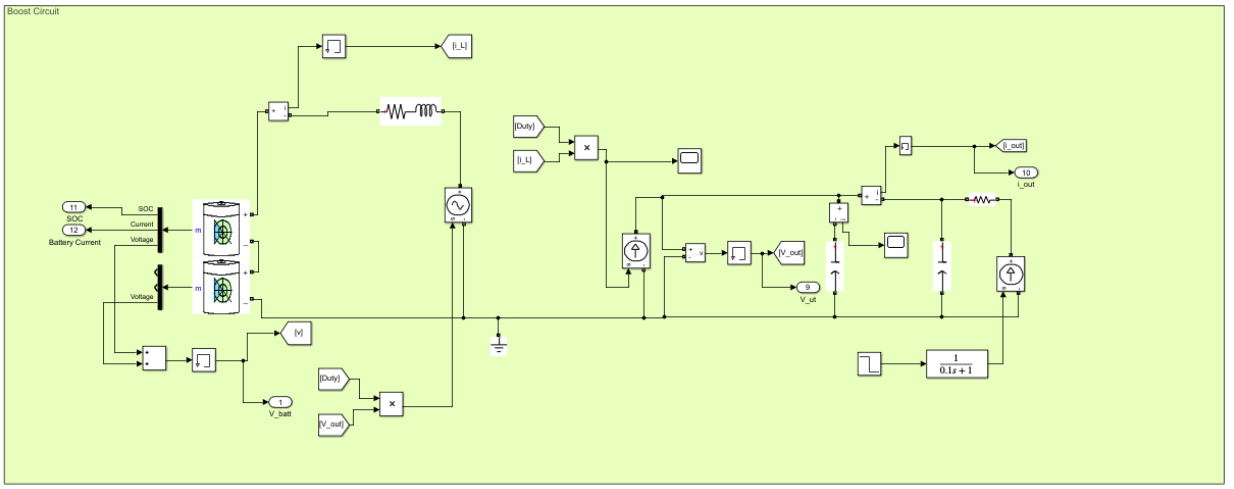

Figure C.1: Simulink Model of average boost converter

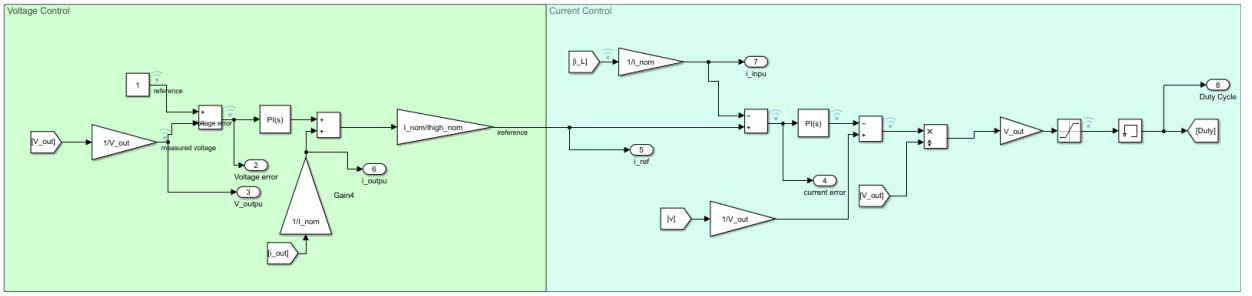

Figure C.2: Simulink model of voltage and current control

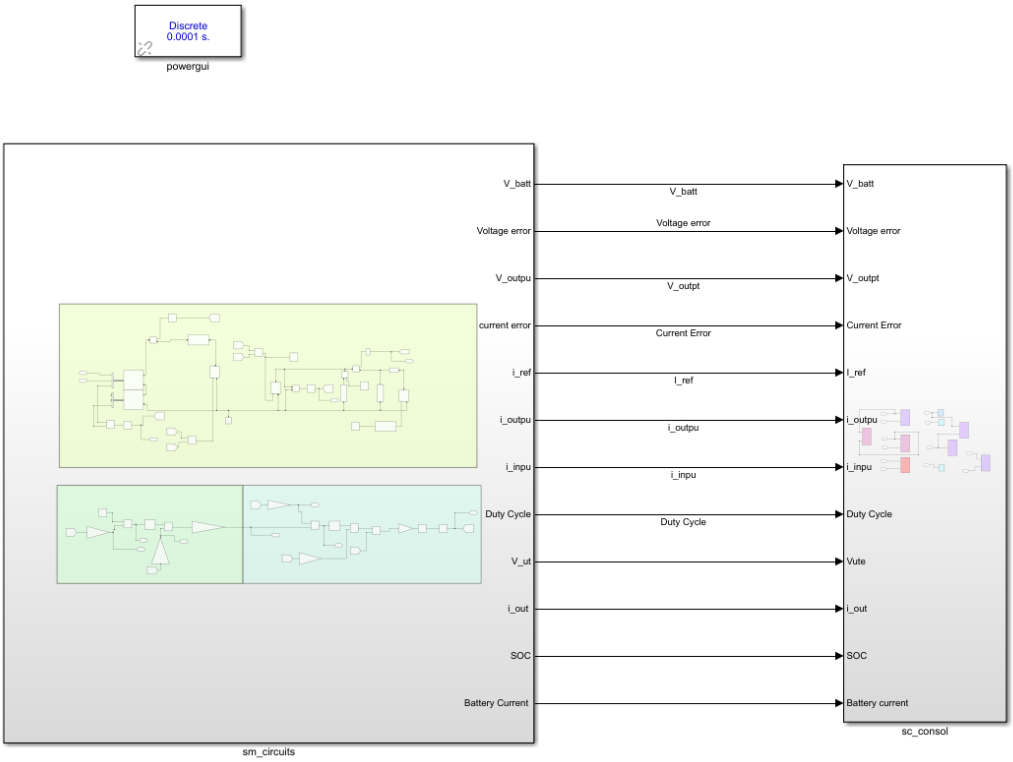

Figure C.3: Simulink model setup prepared for real time simulations

C.2 Computation Model for section 6.3

Figures C.4 and C.5 presents the computational Simulink model which enabled the results presented in section 6.3. It can be observed that the current signal IK and voltage signal V_{out} are retrieved from the boost average model and used in the implemented discretization algorithm.

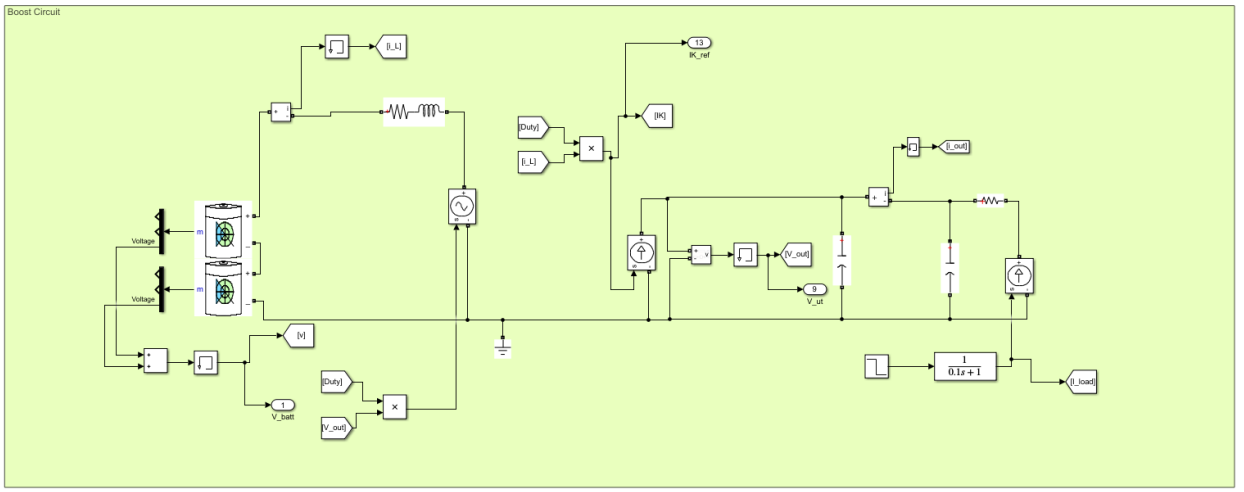

Figure C.4: Simulink model of average boost converter with discretization signals retrieved

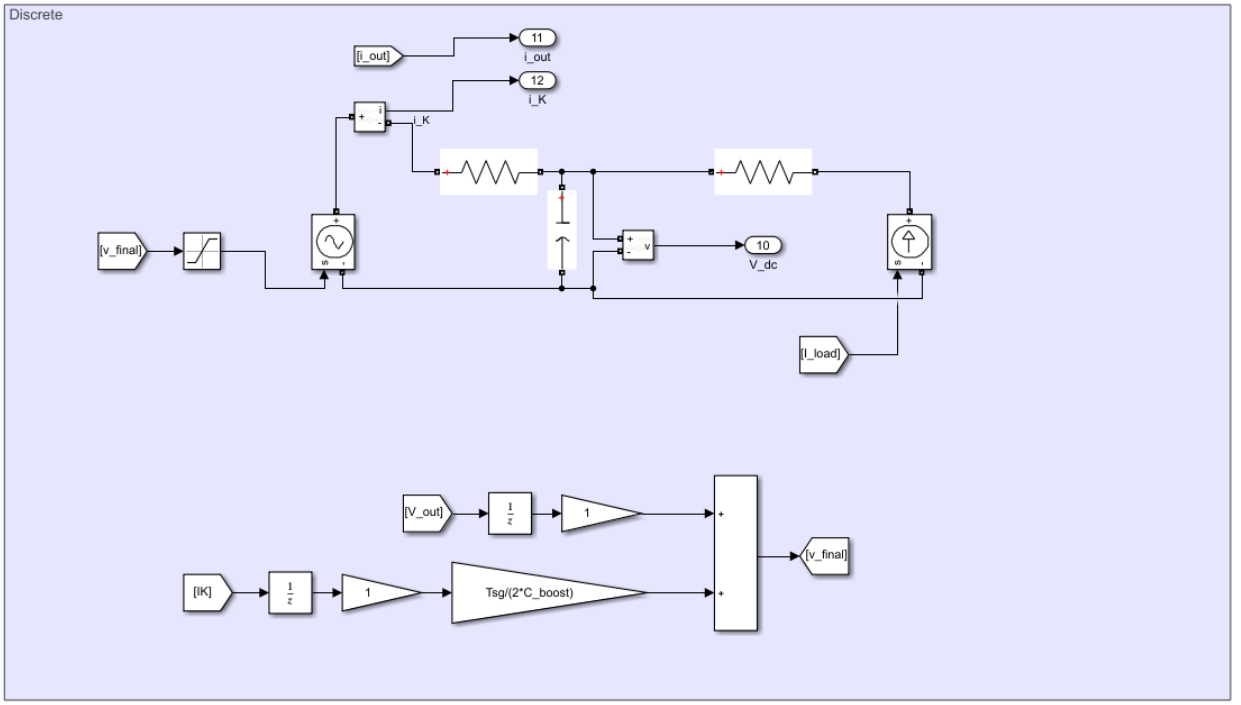

Figure C.5: Simulink model with the implementation of the discretization algorithm

C.3 Computation Model for section 6.4

In section 6.4, noise is introduced to the model. This can be observed in figure C.6 as an addition to i_{out} and V_{out}.

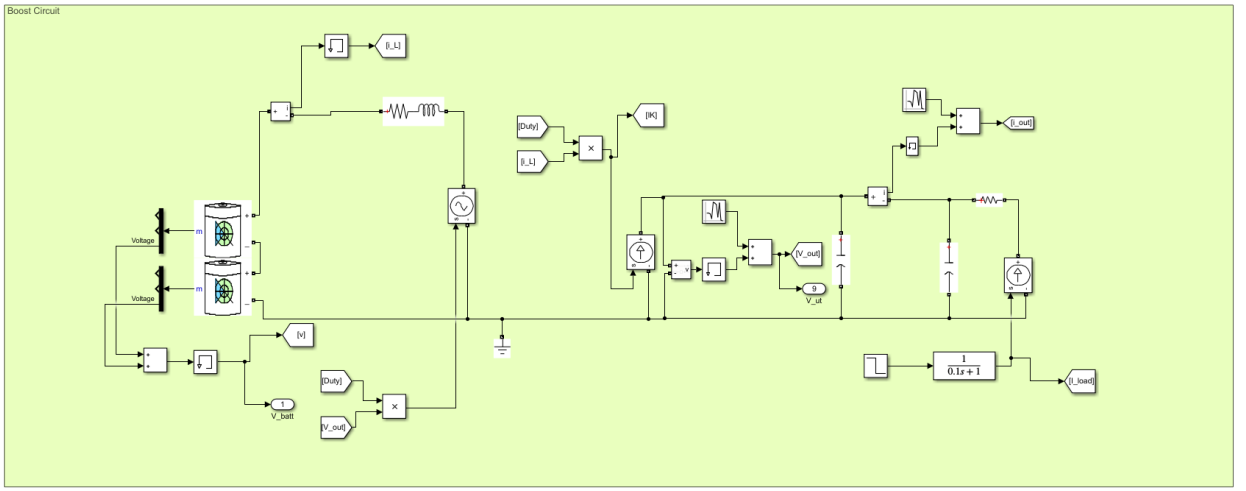

Figure C.6: Simulink model of average boost converter with the implementation of noise at the current and voltage output

Appendix D

MATLAB Script for Simulink Parameters

```
%SYSTEM PARAMETERS

%Base Parameters

Tsg = 100e-6;
Pb=20e3; %VA
V_dc= 650; %V
f=50; %Hz
wb=2*pi*f;
Fsw=10*10^3;
Ta=0.15*10^(-3);


%Battery Bank
V_nom1cell = 3.7; %Nominal voltage in 1 cell [V]
V_nom = 48; %V
n_s = 13; %Number of cells in series
Q_nom = 1559.25; %Nominal capacitance [Ah]
```

```
n_p = 600; %Number of cells in parallel
Z_int = 0.91; %total impedance

%Boost Converter
V_out = V_dc; %[V]
V_in = 300;
gain=V_out/V_in;
D_nom= (gain-1)/gain;
D = D_nom; %Duty Cycle
I_nom = Pb/V_out;
Ihigh_nom = Pb/V_in;
alpha = 0.04; %current ripple
deltaI = alpha*Ihigh_nom;
I_LB= deltaI/2;
T_s = 1/(Fsw);
L_boost=(T_s*V_out)/(2*I_LB)*D*(1-D);
%Resistor asummed to be 1 perscent of losses
R_boost=V_in^2/Pb*0.005;
alpha_V=0.05;
deltaV=alpha_V*V_out;
R_load = V_out^2/Pb;
C_boost= V_out*D*T_s/(deltaV*R_load);
Zbase_boost=V_out/I_nom;
Cbase_boost = 1/(wb*Zbase_boost);
Cpu_boost = C_boost/Cbase_boost;

%Boost Current Control
Ta_bd = 2e-4;
tau_boost=L_boost/R_boost;
Kp_boost=L_boost/(2*wb*Ta_bd);
Ki_boost=Kp_boost*wb/tau_boost;

%Boost voltage Control
p_bd=1/(2*Ta_bd);
z_bd=p_bd/5;
wm=sqrt(p_bd*z_bd);

Kpv_boost=(wm*Cpu_boost)/wb;
```

```
Kiv_boost=z_bd*Kpv_boost;
```